PAPER

Check for updates

Solvation structures of potassium bis(trifluoromethylsulfonyl)imide–glyme highly concentrated electrolytes and cycling on organic cathodes

Pieter Geysens, [ID] [a] Roy Heyns,[a] Robert Markowski,[b] Johannes Ingenmey,[c] Luc Van Meervelt,[a] Alexandru Vlad, [ID] [b] Barbara Kirchner, [ID] [c] Jan Fransaer [ID] [d] and Koen Binnemans [ID] *[a]

The physicochemical properties of highly concentrated electrolytes consisting of potassium bis(trifluoro-methylsulfonyl)imide in oligo(ethyleneglycol) dimethyl ethers (glymes) are reported. The solvation structures were analyzed by Raman spectroscopy, single crystal X-ray diffraction, and theoretical calculations revealing significant ion-pairing at high concentrations especially for the shorter glymes, leading to them being classified as poor solvate ionic liquids with the general formula $[K(L)_n][Tf_2N]$ (L = G1, G2, G3, or G4; n = 2, 3 or 4). $[K(G1)_2][Tf_2N]$ and $[K(G2)_2][Tf_2N]$ had a sufficiently high ionic conductivity and were assessed as potential electrolytes in next-generation potassium-ion batteries. They were subjected to galvanostatic cycling on the new organic cathode material K_2–Co–PTtSA (PTtSA = benzene-1,2,4,5-tetra-methyl-sulfonamide). The results show a significantly improved capacity retention with these electrolytes, especially $[K(G2)_2][Tf_2N]$ (91% after 200 cycles), compared to a benchmark electrolyte consisting of 1 mol L^{-1} KPF_6 in a mixture of ethylene carbonate and propylene carbonate (19% after 200 cycles). However, the performance at high C-rates was worse due to the high viscosities of highly concentrated electrolytes. This work shows that highly concentrated electrolytes and solvate ionic liquids can be promising electrolytes for next-generation potassium-ion batteries but can be further improved to reduce their viscosity and increase their ionic conductivity.

Introduction

In the last decade, the focus on battery research has been shifted from lithium-ion batteries (LIBs) to sodium-ion batteries[1] (NIBs) and rechargeable magnesium metal batteries[2] (RMBs) due to the higher abundance and favorable properties of sodium and magnesium. More recently, potassium-ion batteries (KIBs) have also entered the scene of secondary battery research because of some desirable properties of the element potassium.[3,4] The reduction potential of the K^+/K couple in organic electrolytes is even more negative than that of the Li^+/Li couple, which opens the door to the design of high-voltage batteries (>4 V class) when combined with an appropriate cathode material.[5,6] Furthermore, because of its lower Lewis acidity, the K^+ cation interacts less strongly with its environment (solvents and electrode materials) compared to Li^+, Na^+ and especially Mg^{2+}, leading to higher ionic conductivities of the electrolytes and faster intercalation kinetics at the electrolyte–electrode interfaces.[5,7,8] In contrast to Na^+, K^+ can also intercalate reversibly at reasonably high capacities (244 mAh g^{-1}) into graphite anodes.[5] Potassium-containing electrolytes have been much less explored than new anode and cathode materials for reversible K^+ intercalation. Many potassium salts of interest for batteries such as KBF_4 and $KClO_4$ are barely soluble in typical carbonate ester solvents such as ethylene carbonate (EC) and propylene carbonate (PC), due to their high lattice energy and the weak solvation of K^+ cations.[6,8] A "benchmark" electrolyte for KIBs is KPF_6 in a mixture of EC and PC because of similarities with analogous Li^+ and Na^+ electrolytes and good passivation properties of the PF_6^- anion with Al current collectors.[9] Unfortunately, batteries with this electrolyte typically suffer from large irreversible capacities in the initial cycles and low coulombic efficiencies due to poor

[a]Department of Chemistry, KU Leuven, Celestijnenlaan 200F, P.O. box 2404, B-3001 Leuven, Belgium. E-mail: Koen.Binnemans@kuleuven.be
[b]Institute of Condensed Matter and Nanosciences, UC Louvain, Place L. Pasteur 1, B-1348 Louvain-la-Neuve, Belgium
[c]Mulliken Center for Theoretical Chemistry, University of Bonn, Bonn D-53115, Germany
[d]Department of Materials Engineering, KU Leuven, Kasteelpark Arenberg 44, B-3001 Leuven, Belgium

solid electrolyte interface (SEI) formation on the anode.[10–13] Therefore, researchers are focusing more and more on the development of alternative electrolytes that do not have these issues of passivation and excessive chemical decomposition. One of the possible candidates are *highly concentrated electrolytes* (HCEs), which have been extensively reported on in the context of lithium-, sodium- and magnesium-based batteries.[14–16] HCEs are known to have several advantages compared to their dilute counterparts, such as increased oxidative and reductive stability, non-corrosiveness towards Al current collectors, decreased flammability and volatility, high charge carrier density, fast electrode reactions and decreased polysulfide solubility.[17] Most importantly, because the salt anions are mostly coordinated to the cations in *contact ion pairs* (CIPs) or *aggregate* (AGG) solvate structures, they preferentially decompose over the solvent molecules, leading to an anion-derived robust inorganic SEI.[18–22] Studies on potassium-containing HCEs are still scarce. Xiao *et al.* were the first to report on the application of a HCE consisting of potassium bis(fluorosulfonyl)imide (KFSI) in 1,2-dimethoxyethane (DME, G1, monoglyme) with a molar ratio of 1 : 2, in an anode-less Cu|K battery.[23] They achieved stable cycling of dendrite-free potassium metal on the copper current collector with a coulombic efficiency of 99%, indicating the formation of a stable and thin SEI. The overall electrochemical window of the HCE was 5 V, which allowed for coupling with a high-voltage Prussian Blue (KPB) cathode. Later, Hosaka *et al.* extended this work to the use of this HCE in a graphite|KFSI/DME|KPB full cell and achieved an impressive >85% capacity retention after 101 cycles with an average coulombic efficiency of 99.3%.[24] Replacing the DME solvent with longer glymes such as diethylene glycol dimethyl ether (diglyme, G2) or triethylene glycol dimethyl ether (triglyme, G3) was found to significantly enhance the oxidative stability of the HCEs, resulting in an increased cycling stability of full cells.[25] Xu *et al.* employed the strategy of adding a non-coordinating fluorinated diluent (1,1,2,2-tetrafluoro-1-(2,2,2-trifluoroethoxy)-ethane, TFETFE) to the KFSI/glyme HCE in order to form a *localized high concentration electrolyte* (LHCE).[26] They achieved an unprecedented 83% capacity retention after 2000 cycles for K|KPB cells at a cut-off voltage of 4.3 V. Mandai *et al.* prepared several equimolar complexes of potassium salts with pentaethylene glycol dimethyl ether (pentaglyme, G5) and reported phase diagrams, solvate structures and physicochemical properties.[27] Some of the complexes exhibited ionic-liquid-like behavior and could be classified as so-called *solvate ionic liquids* (SILs) or *liquid metal salts* (LMS). However, the authors did not report any electrochemical properties. Zeng *et al.* prepared a HCE (3.3 mol L^{-1}) consisting of KFSI in trimethyl phosphate (TMP), which resulted in a non-flammable electrolyte for safe KIBs.[28] The authors achieved stable cycling of both graphite anodes and Prussian Blue cathodes with this HCE due to the formation of a stable and robust anion-derived SEI.

Here we report on the solvation structures such as *solvent separated ion pairs* (SSIPs), *contact ion pairs* (CIPs), and *aggre-gates* (AGGs) of several HCEs consisting of potassium bis(trifluoromethylsulfonyl)imide (KTf$_2$N, KTFSI) dissolved in glymes (G1, G2, G3, and G4), studied using Raman spectroscopy, single crystal X-ray diffraction (SCXRD), density functional theory (DFT) calculations, and molecular dynamics (MD) studies. Some of these HCEs can be classified as SILs and the dynamic viscosity, density, potassium concentration, and melting point or glass transition temperature of the complexes [K(L)$_n$][Tf$_2$N] (L = G1, G2, G3, or G4; n = 2, or 3) are also reported. As a proof of concept, we demonstrate the charge–discharge cycling results of [K(G1)$_2$][Tf$_2$N] and [K(G2)$_2$][Tf$_2$N], with the organic cathode material K$_2$–Co–PTtSA (PTtSA = benzene-1,2,4,5-tetra-methylsulfonamide) in a coin-cell configuration.

Experimental

Materials and synthesis

Potassium bis(trifluoromethylsulfonyl)imide (KTf$_2$N, KTFSI, 99.5%) was purchased from Solvionic (Toulouse, France) and was dried at 120 °C for 24 h on a vacuum line prior to use. 1,2-Dimethoxyethane (monoglyme, G1, 99+%, extra dry over molecular sieves) and 1-methoxy-2-(2-methoxyethoxy)ethane (diglyme, G2, 99+%, extra dry over molecular sieves) were purchased from Fisher Scientific (Brussels, Belgium) and were used as received. 1,2-Bis(2-methoxyethoxy)ethane (triglyme, G3, 99%) and bis[2-(2-methoxyethoxy)ethyl] ether (tetraglyme, G4, 99%) were purchased from Fisher Scientific (Brussels, Belgium) and dried prior to use over freshly activated molecular sieves (3 Å, 1 to 2 mm) which were purchased from Alfa Aesar (Belgium). The water content of the glymes was measured using a Mettler-Toledo C30S coulometric Karl Fischer titrator and was found to be lower than 50 ppm, in accordance with the specification provided by the manufacturer. Ferrocenium hexafluorophosphate (FcPF$_6$, 97%) was purchased from Merck (Darmstadt, Germany) and was used as received. Ferrocene (Fc, purum, ≥98%) was purchased from Fluka (Bucharest, Romania) and was used as received. *N*-Butyl-*N*-methylpyrrolidinium bis(trifluoromethylsulfonyl)imide ([BMP][Tf$_2$N], 99%) was purchased from IoLiTec (Heilbronn, Germany) and was dried at 110 °C for 48 h on a vacuum line prior to use. Storage of the reagents and all the manipulations involving contact of the chemicals with the atmosphere were performed in an argon-filled glovebox with oxygen and water concentrations below 1 ppm. The solvate ionic liquids were prepared by adding a stoichiometric amount of glyme to KTf$_2$N in glass vials, which were closed with airtight screwcaps afterwards, and subsequently heating the mixture under stirring until a homogeneous liquid was obtained. The liquids were then allowed to cool down to ambient glovebox temperature (~28 °C).

Methods

Melting points were determined using a Mettler-Toledo DSC-1 instrument at a heating rate of 10 °C min^{-1} under a helium

atmosphere. Aluminium crucibles were filled with samples of electrolyte (3 to 12 mg) inside an argon-filled glovebox and sealed to prevent contact with air. The samples were cycled twice (heating first) between −80 °C and 100 °C. The melting point values determined in the second cycle are reported. Thermogravimetric analysis (TGA) was performed with a TA Instruments TGA Q500 at a heating rate of 5 °C min⁻¹ under a nitrogen atmosphere with a flow rate of 60 mL min⁻¹. The sample size was typically between 5 and 10 mg. In order to make the TGA traces of the different samples directly comparable, the data (mass *vs.* time) were normalized by dividing by their initial mass values. The data on the *y*-axis are expressed as the remaining fraction of the initial sample mass (in %). The viscosity and density of the electrolytes were measured with a Lovis 2000 ME rolling-ball microviscometer and a DMA 4500 M density meter, respectively. To avoid contact with air, the samples were transferred from their sealed argon-filled containers to a syringe and subsequently injected into the capillaries or density chamber of the device. The temperature during both the viscosity and density measurements was controlled using the internal thermostat of the device. The specific ionic conductivity of the electrolytes was measured using a Mettler-Toledo SevenCompact Cond S230 conductivity meter equipped with an InLab 751-4 mm glass probe with two platinum poles. The instrument was calibrated using aqueous standards with a known specific ionic conductivity. The probe was submerged in the electrolytes at ambient temperature (approximately 25 °C) and the setup was allowed to stabilize. Contact of the samples with ambient air was unavoidable during the measurement. FT-Raman spectra were recorded between 3500 cm⁻¹ and 50 cm⁻¹ on a Bruker Vertex 70 spectrometer with a RamII Raman module and a liquid-nitrogen-cooled germanium diode detector. Each measurement consisted of 64 scans at a resolution of 2 cm⁻¹ with a 1064.38 nm laser (Nd:YAG) at a power of 500 mW. Samples were measured inside 2 mL glass vials that were filled inside the glovebox and subsequently closed with airtight screwcaps. Single crystal X-ray diffraction measurements were performed on [K(G3)$_2$][Tf$_2$N]. Single crystals were obtained by slow cooling of a concentrated solution of the complex in G3. A suitable crystal was selected and placed on a Bruker D8 Venture diffractometer. The crystal was kept at 100(2) K during data collection. Using Olex2,[29] the structure was solved with the SHELXT[30] structure solution program using intrinsic phasing and refined with the SHELXL[31] refinement package using least squares minimization. All H atoms were placed in calculated positions and treated as riding on their parent atoms, with C–H = 0.93–0.98 Å and U_{iso}(H) = 1.2 or 1.5 U_{eq}(C). The asymmetric unit consists of two half Tf$_2$N⁻ anions (the two remaining halves are generated by inversion centers) and are disordered over several positions. The first half was refined with two positions, but the second half was too disordered to refine. Therefore, the solvent mask procedure was used during the refinement. A cavity of 311 Å³ with 140 electrons (Tf$_2$N⁻ = 138 electrons) therein was used. All the electrochemical measurements were performed inside an argon-filled glovebox with

water and oxygen concentrations below 1 ppm. Cyclic voltammograms (CVs) were obtained using an Autolab PGSTAT302N potentiostat and Nova 2.1 software. The working electrodes for CV were pieces of silicon wafer, coated with 500 nm of silica, 10 nm of titanium and 100 nm of platinum (Imec, Belgium) (surface area of 0.3 cm²), the counter electrode was a larger piece of platinum-coated silicon wafer (surface area of approx. 1.0 cm²) and the scan rate was 10 mV s⁻¹. The reference electrode consisted of a platinum wire, submerged in a solution of ferrocene (Fc) and ferrocenium hexafluorophosphate (FcPF$_6$) (5 mmol L⁻¹ each) in the ionic liquid *N*-butyl-*N*-methyl-pyrrolidinium bis(trifluoromethylsulfonyl)imide ([BMP][Tf$_2$N]), contained inside a fritted glass tube (referred to as Fc⁺/Fc). The CVs were started at open circuit potential (OCP) and are uncorrected for ohmic drop. The galvanostatic cycling tests were carried out using 2025-type coin cells with a 13 mm diameter active carbon fabric as the counter/reference electrodes and glass microfiber filters as the separators. The positive electrode composition was made by hand-grinding 50 wt% active material (K$_2$–Co–benzene-1,2,4,5-tetra-methylsulfonamide) with 40 to 10 wt% conductive carbon (Super P) and 10 wt% PTFE as a binder.[32] The electrodes were manufactured by applying the composite powder to the positive side of the coin cell case (CR 2032, AISI 316L stainless steel) and compacting with a stainless-steel disk. The active material loading is approximately 1.5–2 mg, with a surface density of approximately 3 mg cm⁻² (corresponding to approx. 6 mg cm⁻² of the composite), with an electrode thickness of approx. 0.15 mm. The electrode porosity was not quantitatively evaluated. However, SEM observations indicate that the electrode is slightly compressed while retaining sufficient porosity, enabling effective electrolyte penetration throughout the composite electrode. At room temperature, galvanostatic charge/discharge experiments were conducted using a Neware battery testing equipment. As electrolytes, 1 mol L⁻¹ KPF$_6$ in EC : PC, [K(G1)$_2$][Tf$_2$N] and [K(G2)$_2$][Tf$_2$N] were used. A GF/D glass-fiber separator was used, and 150 μL of electrolyte was added to each cell. The long-term stability tests were performed at a cycling rate of C/10.

Theoretical calculations

Classical molecular dynamics (MD) simulations were performed using the LAMMPS program package (version of 23 June 2022).[33] The composition and final box dimensions of the simulated systems are given in the SI (Table S6). OPLS-AA[34] force field parameters were employed for the glymes, the Tf$_2$N⁻ anion, and the K⁺ cation.[35] Geometric mixing rules were applied for non-bonded interactions between unlike atoms.[36] The cutoff for Lennard-Jones and coulombic interactions was set to 1.2 nm. Initial configurations were created randomly using the PACKMOL tool.[37] Bulk simulations of G*n*–KTf$_2$N with *n* = 1–4 at compositions of 1 : 2, 1 : 3, and 1 : 4 were carried out in cubic boxes, employing periodic boundary conditions in all directions. The systems were equilibrated over a total simulation time of 35 ns in the NVE, NpT, and NVT ensemble. After an initial energy minimization, the system was

simulated for 250 ps in the NVE ensemble with added velocity scaling corresponding to a temperature of 500 K. Afterwards, the systems were simulated for 14 ns in the NpT ensemble. The Nosé–Hoover chain thermostat and barostat were applied to achieve a constant pressure of 1.01325 bar and a temperature of 350.15 K.[38,39] The average volume of the latter 10 ns was then used as the final box volume for the subsequent equilibration of 21 ns in the NVT ensemble. Finally, a production run of 10 ns was carried out in the NVT ensemble. The timestep was set to 1.0 fs and every 1000th step was saved in a trajectory for further processing.

Quantum chemical calculations were carried out at the DFT level of theory using the ORCA 5.0 program package.[40] The B3LYP functional was employed in combination with the def2-TZVP basis set. The D3 dispersion correction[41,42] was applied to account for London dispersion interactions. Grimme's geometrical counterpoise[43] correction was used to deal with the inter-molecular as well as intra-molecular basis set superposition error. Tight SCF convergence criteria were applied for all calculations. Harmonic frequencies were calculated as analytical derivatives of the energy gradient to ensure the absence of imaginary modes. Electrochemical reduction and oxidation potentials were calculated following the adiabatic thermodynamic cycle method eqn (1) and eqn (2):[44,45]

$$U_{\mathrm{red}}(R) = \frac{E(R) - E(R^-)}{nF} - U_{\mathrm{ref}} \tag{1}$$

$$U_{\mathrm{ox}}(R) = \frac{E(R^+) - E(R)}{nF} - U_{\mathrm{ref}} \tag{2}$$

where $E(R)$, $E(R^-)$, and $E(R^+)$ are the electronic energy of compound or complex R in its neutral, reduced, and oxidized forms, respectively, and $U_{\mathrm{ref}} = 1.549$ V to account for the difference between the absolute potential scale and K/K$^+$. The conductor-like polarizable continuum model (CPCM) was employed to implicitly account for solvation effects.[46] The relative permittivity was set to each glyme's respective experimental value (ε_{r}(G1) = 7.1, ε_{r}(G2) = 7.4, ε_{r}(G3) = 7.6, and ε_{r}(G4) = 7.8), while all other CPCM parameters were kept at their default values.[47]

Synthesis and characterization data of complexes

[K(G1)$_2$][Tf$_2$N]. A mixture of KTf$_2$N (1.000 g, 3.132 mmol) and G1 (0.565 g, 6.265 mmol) was stirred inside a closed glass vial at 60 °C under argon until complete dissolution of the solid. Upon cooling, the mixture remained a homogeneous liquid and [K(G1)$_2$][Tf$_2$N] (1.565 g, 3.132 mmol, 100% yield) was isolated as a clear colorless viscous liquid. (FT-Raman shifts/cm^{-1}): 2999, 2954, 2930, 2903, 2832, 1476, 1455, 1246, 1140, 860, 744, 407, 366, 353, 339, 327, 314, 298, 280, 119. Glass transition point: −56 °C.

[K(G1)$_3$][Tf$_2$N]. A mixture of KTf$_2$N (1.001 g, 3.136 mmol) and G1 (850 g, 9.432 mmol) was stirred inside a closed glass vial at 60 °C under argon until complete dissolution of the solid. Upon cooling, the mixture remained a homogeneous liquid and [K(G1)$_3$][Tf$_2$N] (1.851 g, 3.139 mmol, 100% yield)

was isolated as a clear colorless viscous liquid. (FT-Raman shifts/cm^{-1}): 2996, 2952, 2930, 2901, 2831, 1476, 1454, 1287, 1245, 1140, 860, 743, 406, 365, 339, 326, 313, 298, 280, 119. Melting point: −33 °C.

[K(G1)$_4$][Tf$_2$N]. A mixture of KTf$_2$N (0.999 g, 3.129 mmol) and G1 (1.130 g, 12.539 mmol) was stirred inside a closed glass vial at 60 °C under argon until complete dissolution of the solid. Upon cooling, the mixture remained a homogeneous liquid and [K(G1)$_4$][Tf$_2$N] (2.129 g, 3.132 mmol, 100% yield) was isolated as a clear colorless viscous liquid. (FT-Raman shifts/cm^{-1}): 2993, 2950, 2928, 2900, 2830, 2726, 1476, 1453, 1245, 1140, 860, 743, 406, 366, 339, 326, 313, 297, 280, 119. Melting point: not observed.

[K(G2)$_2$][Tf$_2$N]. A mixture of KTf$_2$N (1.002 g, 3.139 mmol) and G2 (841 g, 6.265 mmol) was stirred inside a closed glass vial at 60 °C under argon until complete dissolution of the solid. Upon cooling, the mixture remained a homogeneous liquid and [K(G2)$_2$][Tf$_2$N] (1.843 g, 3.137 mmol, 100% yield) was isolated as a clear colorless viscous liquid. (FT-Raman shifts/cm^{-1}): 2950, 2901, 2835, 2751, 1476, 1450, 1336, 1282, 1245, 1139, 868, 840, 743, 573, 406, 326, 313, 298, 279, 119. Melting point: −8 °C.

[K(G2)$_3$][Tf$_2$N]. A mixture of KTf$_2$N (0.998 g, 3.126 mmol) and G2 (1.258 g, 9.376 mmol) was stirred inside a closed glass vial at 60 °C under argon until complete dissolution of the solid. Upon cooling, the mixture remained a homogeneous liquid and [K(G2)$_3$][Tf$_2$N] (2.256 g, 3.126 mmol, 100% yield) was isolated as a clear colorless viscous liquid. (FT-Raman shifts/cm^{-1}): 2949, 2895, 2833, 2751, 1476, 1452, 1282, 1244, 1139, 868, 840, 742, 572, 405, 326, 313, 298, 279, 167, 119. Melting point: −4 °C.

[K(G3)$_2$][Tf$_2$N]. A mixture of KTf$_2$N (1.001 g, 3.136 mmol) and G3 (1.120 g, 6.284 mmol) was stirred inside a closed glass vial at 60 °C under argon until complete dissolution of the solid. Upon cooling, the mixture crystallized and [K(G3)$_2$][Tf$_2$N] (2.121 g, 3.139 mmol, 100% yield) was isolated as a clear colorless crystalline solid. (FT-Raman shifts/cm^{-1}): 2944, 2925, 2899, 2852, 2826, 1478, 1448, 1273, 1244, 1144, 1134, 872, 840, 741, 341, 314, 305, 281, 123, 102. Melting point: 45 °C.

[K(G4)][Tf$_2$N]. A mixture of KTf$_2$N (1.000 g, 3.132 mmol) and G4 (0.696 g, 3.132 mmol) was stirred inside a closed glass vial at 60 °C under argon until complete dissolution of the solid. Upon cooling, the mixture crystallized and [K(G4)][Tf$_2$N] (1.696 g, 3.132 mmol, 100% yield) was isolated as a clear colorless crystalline solid. (FT-Raman shifts/cm^{-1}): 2952, 2903, 2864, 2841, 1477, 1456, 1280, 1244, 1141, 866, 835, 742, 558, 398, 341, 326, 314, 298, 279, 121. Melting point: 36 °C.

[K(G4)$_2$][Tf$_2$N]. A mixture of KTf$_2$N (0.999 g, 3.129 mmol) and G4 (1.392 g, 6.262 mmol) was stirred inside a closed glass vial at 60 °C under argon until complete dissolution of the solid. Upon cooling, the mixture remained a homogeneous liquid and [K(G4)$_2$][Tf$_2$N] (2.391 g, 3.130 mmol, 100% yield) was isolated as a clear colorless viscous liquid. (FT-Raman shifts/cm^{-1}): 2891, 2834, 1476, 1452, 1337, 1281, 1243, 1139, 866, 836, 741, 572, 405, 339, 326, 312, 297, 279, 165, 120. Melting point: 19 °C.

Results and discussion

Physicochemical properties of glyme–KTf$_2$N binary mixtures

When KTf$_2$N is dissolved in glymes, the K$^+$ cations are solvated by the ether oxygen atoms of the glyme molecules, leading to the formation of solvate complexes. Several possible solvate complex structures are defined, depending on the number of anions in the primary coordination shell around the K$^+$ cations (Fig. 1). *Solvent separated ion pairs* (SSIPs) are structures in which the K$^+$ cations are completely separated from the anions by a primary coordination shell consisting of only solvent molecules. *Contact ion pairs* (CIPs) are neutral complexes in which the K$^+$ cations are solvated by solvent molecules and one anion. Depending on the coordination of the anion, CIP I and CIP II can be distinguished, where the anion coordinates in a monodentate or bidentate manner, respectively. In *aggregates* (AGGs), several K$^+$ cations are linked together by two (AGG I) or three (AGG II) anions, resulting in large polymeric coordination networks. In any solution of KTf$_2$N in glymes, these different solvation structures exist in equilibrium with each other due to the kinetically labile nature of alkali metal ion complexes.

Mixtures of the glymes monoglyme (G1), diglyme (G2), triglyme (G3), and tetraglyme (G4) with potassium bis(trifluoromethylsulfonyl)imide (KTf$_2$N) with glyme : KTf$_2$N ratios ranging from 50 : 1 to 1 : 1 were prepared. It was found that even at high concentrations of KTf$_2$N, homogeneous liquid mixtures were obtained, indicating a high solubility of this salt in the glyme solvents. This can be explained by the excellent electron-withdrawing properties of the –SO$_2$CF$_3$ groups in the anion resulting in efficient electron delocalization. For the G1

and G2 series of mixtures, only at a 1 : 1 ratio, inhomogeneous (liquid + solid) mixtures were observed, indicating a solubility limit. For the G3 series of mixtures, crystals were observed at a 4 : 1 ratio and below and the 2 : 1 ratio mixture was a homogeneous solid. These crystals were analyzed using single crystal X-ray diffraction and it was revealed that the crystalline solid was the solvate complex [K(G3)$_2$][Tf$_2$N] (*vide infra*). For the G4 : KTf$_2$N series, every mixture was a homogeneous liquid except the 1 : 1 mixture, which was a homogeneous crystalline solid. In order to assess the suitability of these glyme–KTf$_2$N mixtures as electrolytes in batteries, their physicochemical properties such as specific ionic conductivity (σ), dynamic viscosity (η_{dyn}), density (ρ) and potassium-ion concentration were determined. The numerical values are summarized in the SI (Tables S1–S4). A plot of the specific ionic conductivity and the dynamic viscosity *vs.* the glyme : KTf$_2$N ratio is shown in Fig. 2.

The specific ionic conductivity is a very important parameter to describe an electrolyte, since it has a significant influence on the current densities that can be achieved during charge–discharge cycling experiments, and therefore the C-rate performance (*vide infra*). The specific ionic conductivity is determined by two factors: (1) the total concentration of charge carriers (ions) and (2) the mobility of those charge carriers. The mobility, in turn, depends on the dynamic viscosity of the electrolyte and the nature of the solvate species that are present in solution. Neutral species such as contact ion pairs (CIPs) are not attracted to the electrodes as opposed to charged species such as solvent separated ion pairs and are therefore less mobile. The solvation in these glyme–KTf$_2$N electrolytes is extensively discussed below. In Fig. 2a, a typical maximum curve can be observed for the conductivity as a func-
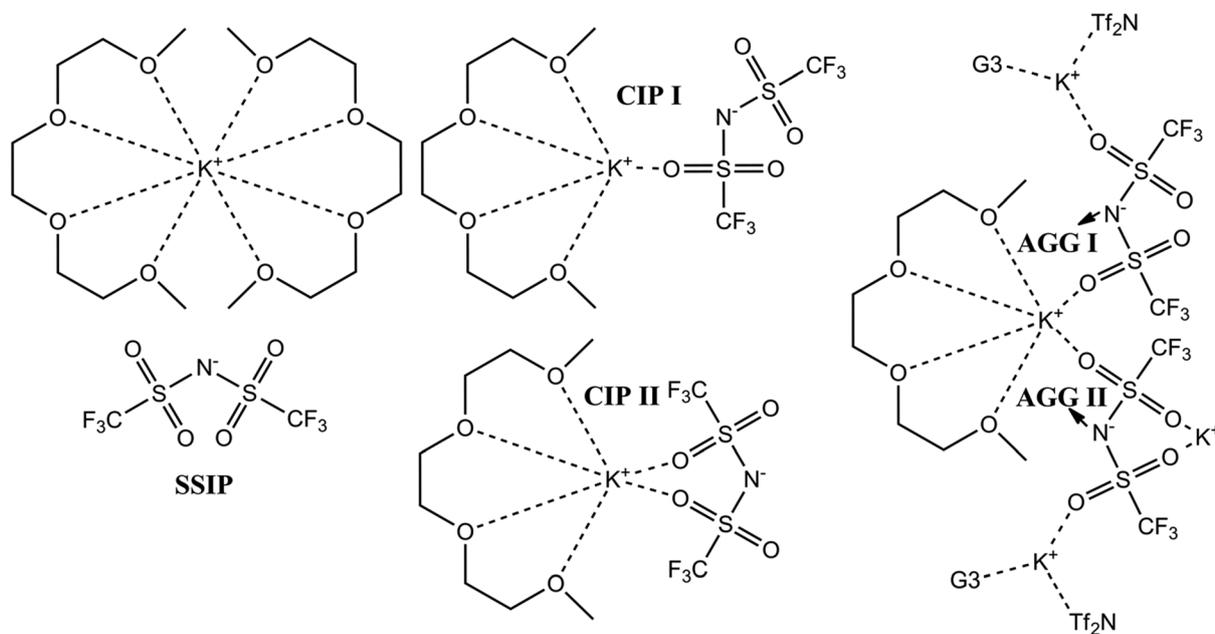

Fig. 1 Schematic representation of the three main solvated species in KTf$_2$N–triglyme binary mixtures: solvent separated ion pairs (SSIP) (left), contact ion pairs (CIP I and CIP II) (middle), and aggregate structures (AGG I and AGG II) (right).
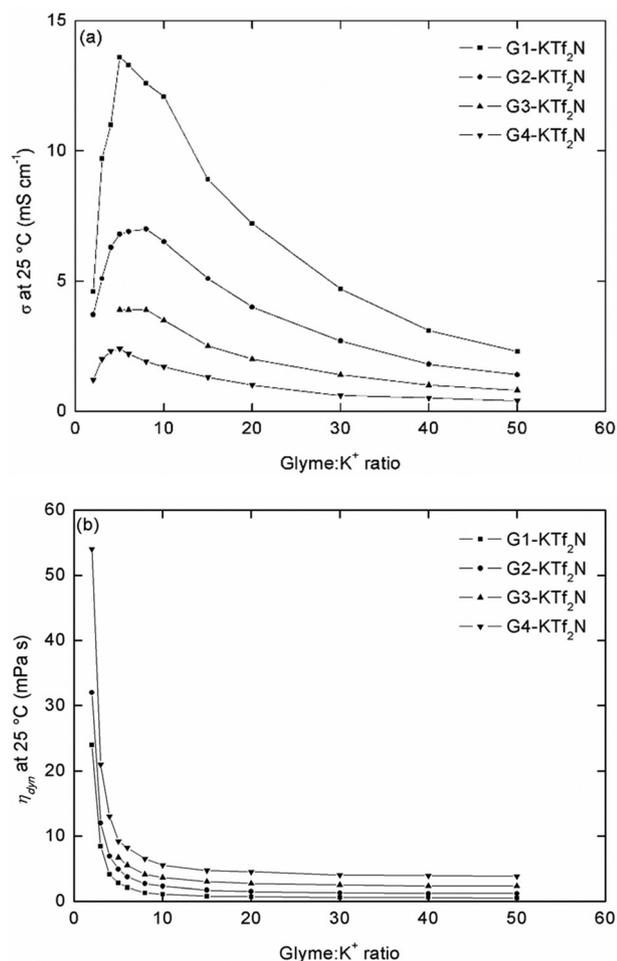
Fig. 2 Specific ionic conductivity (a) and dynamic viscosity (b) of electrolytes *vs.* the glyme : KTf$_2$N ratio, measured at 25 °C. Some datapoints are missing for the G3–KTf$_2$N series because of the presence of crystals in the solution.

tion of the glyme : KTf$_2$N ratio. This can be explained by the two competing factors: the ion concentration and the ion mobility (*i.e.* the viscosity). In relatively dilute conditions, the total ion concentration is dominant over the small increase in viscosity, as the fraction of salt in the electrolytes is increased. This results in an initial increase in conductivity. However, as the salt fraction (ion concentration) is further increased, the viscosity increases more strongly (Fig. 2b), and it becomes the dominant factor, resulting in a decrease of the conductivity. The maximum conductivity is usually reached at the 5 : 1 glyme : KTf$_2$N composition, except for the G2 series of electrolytes, where it is observed at the 8 : 1 composition. However, the change in conductivity compared to the 5 : 1 composition is rather small and within the margin of error of the conductometer. It should be noted that some data points are missing for the G3 series of electrolytes because crystals started forming at ratios of 4 : 1 and below, but it is likely that the conductivity would also have decreased for these compositions in this case. When the different glyme series are com-

pared, it is evident that the conductivity decreases with increasing glyme length. This is because for the same glyme : KTf$_2$N ratio, the K$^+$ concentration is actually lower for the longer glymes due to their increased molar volume. Furthermore, the viscosity of the glymes also increases with increasing chain length (G1: 0.5 mPa s, G2: 1.0 mPa s, G3: 2.0 mPa s, and G4: 3.4 mPa s at 25 °C) due to the stronger dipole and van der Waals interactions. Interestingly, the decrease in conductivity with the glyme : KTf$_2$N ratio is very sharp for the G1 series of electrolytes as opposed to the longer glyme series where it is much more gradual. This can possibly be explained by differences in the solvation structures that are present in solution, *i.e.* a higher degree of CIP and AGG formation in the G1 electrolytes. Overall, the specific ionic conductivities of the glyme–KTf$_2$N electrolytes, especially the G1 and G2 series, are in an acceptable range, even for the highly concentrated examples.

At well-defined stoichiometric ratios of salt and glyme, it might be possible to isolate the solvate complexes in the solid (crystalline) state. Therefore, the most concentrated glyme–KTf$_2$N mixtures were analyzed by differential scanning calorimetry (DSC) in order to determine the melting points (T_m) of these solvate complexes of the general form $[K(Gn)_x][Tf_2N]$ (n = 1–4). The expected coordination number of K$^+$ in glymes is between 8 and 10, according to Mandai *et al.*, so this would correspond to 4 G1, 3 G2, 2 G3 and 2 G4 ligands, if only K$^+$–solvent interactions are considered.[48] Mixtures with a higher glyme : KTf$_2$N ratio were not measured. These solvate complexes are technically considered highly concentrated electrolytes (HCEs) consisting of KTf$_2$N dissolved in glymes. However, if certain criteria are met, these HCEs can also start exhibiting typical behavior associated with ionic liquids, the so-called *solvate ionic liquids* (SILs). Mandai *et al.* have proposed five criteria to distinguish SILs from typical HCEs:[49] (1) they must be solvate compounds between an ion and a ligand(s) in a certain stoichiometric ratio; (2) they must consist entirely of complex ions (solvates) and their counterions in the molten state; (3) they must show no physicochemical properties based on both pure ligands and precursor salts under the applied conditions; (4) they must have a melting point below 100 °C to satisfy the criterion for typical ILs; and (5) they must have a negligible vapor pressure under typical application conditions. In many cases, these criteria are only partially met. In that instance, the HCEs are classified as "poor" SILs. Table 1 summarizes the melting points of the different solvate complexes. For some mixtures, a well-defined melting point was not observed and the glass transition temperature (T_g) is shown in those cases.

In general, the observed melting points of the solvate complexes are well below 100 °C, with most of them even below room temperature (25 °C), thereby satisfying criterion 4. This is typical of complexes with the highly delocalized and flexible bis(trifluoromethylsulfonyl)imide anion that inhibits crystallization. As the glyme chain length increases, the melting point of the corresponding solvate complexes clearly increases as well. For the complexes with G1 ligands, the melting point is either below −30 °C or not observed at all. For the complexes

Table 1 Melting points (T_m) and glass transition (T_g) temperatures

Complex	$T_m{}^a$ (°C)	$T_g{}^a$ (°C)
[K(G1)$_4$][Tf$_2$N]	n.o.	n.o.
[K(G1)$_3$][Tf$_2$N]	−33	n.o.
[K(G1)$_2$][Tf$_2$N]	n.o.	−58
[K(G2)$_3$][Tf$_2$N]	−4	n.o.
[K(G2)$_2$][Tf$_2$N]	−8	n.o.
[K(G3)$_2$][Tf$_2$N]	45	n.o.
[K(G4)$_2$][Tf$_2$N]	19	n.o.
[K(G4)][Tf$_2$N]	36	n.o.

^{a} n.o.: not observed.

with G2 ligands, the melting point is just below 0 °C, and for the G3 and G4 complexes, the melting point is around or just above room temperature (25 °C).

In order to evaluate criterion 5, the thermal stability of the solvate complexes was investigated using dynamic thermogravimetric analysis (TGA) and compared to the pure glymes and pure KTf$_2$N (SI Fig. S1–S4). The pure KTf$_2$N salt does not form any hydrates and is thermally stable up to a temperature of approx. 400 °C, at which point the anion starts to decompose. Upon comparing the TGA traces of the solvate complexes with those of the pure glymes (ligands), an enhanced thermal stability is clearly observed for the complexes over the ligands. However, the overall thermal stability of the G1 and G2 solvate complexes is still quite poor, as most of the glymes are evaporated at a temperature of approx. 100 °C. The complex [K(G3)$_2$][Tf$_2$N] is slightly more stable, and [K(G4)$_2$][Tf$_2$N] and [K(G4)][Tf$_2$N] even more so, where the latter is even thermally stable beyond 100 °C. This trend is of course expected according to the chelate effect of the glyme ligands, as well as their respective boiling points (85, 162, 216 and 275 °C for G1, G2, G3 and G4 respectively). Interestingly, the mass of [K(G1)$_4$][Tf$_2$N] and [K(G1)$_3$][Tf$_2$N] does not decrease to the theoretical value after loss of all ligands. However this can be explained by premature evaporation of the highly volatile G1 ligand before the actual TGA measurement starts. For all the other complexes with longer glyme ligands, the theoretical remaining mass values are reached. [K(G4)][Tf$_2$N] also starts losing ligands at a higher temperature compared to [K(G4)$_2$][Tf$_2$N], so it appears that the second G4 ligand is more weakly coordinated to K$^+$ than the first one. This is also expected, taking into account the significant steric hindrance associated with the coordination of two complete G4 ligands.

Solvation study of glyme–KTf$_2$N binary mixtures

Criteria 1 and 2, which were proposed by Mandai et al., both relate to the solvate structure of the isolated complexes in the solid as well as the liquid state.[49] In general, it is advantageous to study these solvate structures because they provide useful insights into the performance of the batteries that are constructed with these HCEs/SILs. The solvation structure of solids can be revealed using single crystal X-ray diffraction (XRD) techniques and Raman spectroscopy and those of liquids as well using Raman spectroscopy. Theoretical calcu-

lations such as density functional theory (DFT) and molecular dynamics (MD) can also aid to interpret the experimentally observed data.

Of the eight solvate complexes that were prepared, only two were crystalline solids at room temperature: [K(G3)$_2$][Tf$_2$N] and [K(G4)][Tf$_2$N]. Of these two, [K(G4)][Tf$_2$N] had the tendency to form an undercooled liquid upon cooling the melt and form a polycrystalline mass upon crystallizing, so no single crystals of a sufficiently high quality for single crystal XRD were obtained. Good-quality single crystals of [K(G3)$_2$][Tf$_2$N] were readily obtained by slow cooling of the solution in the presence of a slight excess of G3. This was the only complex that was analyzed using single crystal XRD. The unit cell of [K(G3)$_2$][Tf$_2$N] is shown in Fig. 3. The full crystallographic data can be found in the SI (Table S5) and a close-up of the crystal structure is shown in Fig. S5.

[K(G3)$_2$][Tf$_2$N] crystallizes in the triclinic space group $P\bar{1}$. The asymmetric unit consists of a K$^+$ cation, two triglyme molecules and two halves of a Tf$_2$N$^-$ anion. The full Tf$_2$N$^-$ anion is generated by an inversion center. The first half of the Tf$_2$N$^-$ anion is disordered and was refined over two positions. The second half was too disordered to be refined and instead, the solvent mask procedure was used for the refinement. The K$^+$ cations are coordinated by eight oxygen atoms of two perpendicularly oriented triglyme ligands, leading to a total coordination number of eight (Fig. S5). The Tf$_2$N$^-$ anions are not coordinated and are strongly disordered. Therefore, the solvate structure of [K(G3)$_2$][Tf$_2$N] in the crystalline state can be classified as an SSIP-type solvate. This structure is similar to the crystal structure of [Na(G3)$_2$][FSI].[15] The K–O$_{glyme}$ distances vary from 2.7627(15) Å to 2.8381(14) Å.

Although the crystal structure of [K(G4)][Tf$_2$N] could not be determined, it might still be possible to estimate the structure on the basis of the existing literature. Mandai et al. have determined the crystal structure of several potassium salt–glyme solvate complexes with various anions such as Tf$_2$N$^-$, trifluoromethanesulfonate (OTf$^-$), hexafluorophosphate (PF$_6{}^-$) and perchlorate (ClO$_4{}^-$).[27,48] According to the authors, K$^+$ exhibits coordination numbers of 8 to 10 in glymes. G4 is a pentadentate ligand which has five oxygen atoms available for coordi-
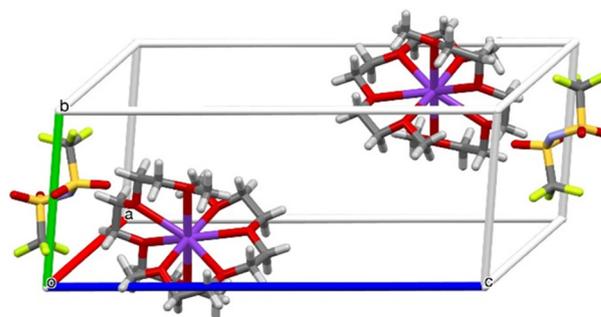

Fig. 3 View of the unit cell of the solvate complex [K(G3)$_2$][Tf$_2$N]. The disorder of the Tf$_2$N$^-$ anion is not shown. Purple, K; red, O; grey, C; white, H; yellow, S; green, F; cyan, N.

nation. Therefore, one G4 ligand is not enough to saturate the first coordination shell of K^+ and the vacant coordination sites will most likely be occupied by oxygen atoms of the Tf_2N^- anion. The solvate complex $[K(G5)][Tf_2N]$ exhibits an AGG solvate structure, where the K^+ cations are linked together one-dimensionally by bridging Tf_2N^- anions, so this is most likely also the case for $[K(G4)][Tf_2N]$. This was also evident from the Raman analysis of this complex (*vide infra*).

The melting point of the solvate complex $[K(G4)_2][Tf_2N]$, 19 °C, was too low for a single crystal XRD study. However, the crystal structure of $[K(G4)_2][PF_6]$ was reported to be an SSIP-type solvate where K^+ is coordinated by ten oxygen atoms of two G4 ligands. Similarly to PF_6^-, Tf_2N^- is also a weakly coordinating anion and it is more bulky. Therefore the SSIP structure is also very likely for $[K(G4)_2][Tf_2N]$ in the solid state.

In the solvate complexes $[K(G1)_3][Tf_2N]$ and $[K(G2)_2][Tf_2N]$, there are only six glyme oxygen atoms available for coordination, so their structure will probably also be an AGG or CIP type in the solid state. In $[K(G2)_3][Tf_2N]$, nine glyme oxygen atoms are available, so this is possibly an SSIP type solvate complex. Unfortunately, it was not possible to analyze these complexes in the solid state by Raman spectroscopy, due to their low melting points.

The solvation structures in liquid as well as solid glyme–alkali salt binary mixtures have been studied intensively using Raman spectroscopy.[27,48,49] Two regions of the Raman spectrum are of particular interest in our case of glyme–KTf_2N binary mixtures. The first region is located in the 780–900 cm^{-1} range, which corresponds to the coupled CH_2 rocking ($r(CH_2)$) and COC stretching ($\nu(COC)$) modes. When solvate complexes are formed between glyme ligands and an alkali cation, a new characteristic band is observed in this region of the Raman spectrum, shifted to higher wavenumbers. This band corresponds to the coupled CH_2 rocking ($r(CH_2)$) and COC stretching ($\nu(COC)$) modes of coordinated glyme molecules, also known as the *ring breathing mode*. Therefore, this band is a useful fingerprint mode to study solvation of alkali salts in glymes. In order to characterize the solvation of KTf_2N in glymes, Raman spectra were recorded for several glyme : KTf_2N molar ratios. The concentration dependence or the Raman spectra for the G1–KTf_2N and G2–KTf_2N binary mixtures in the 780–890 cm^{-1} range is shown in Fig. 4.

The multipeak in the Raman spectrum of pure monoglyme in this region can be deconvoluted into two bands at 822 and 850 cm^{-1} which correspond to the coupled $r(CH_2)/\nu(COC)$ modes of free G1 molecules in different conformations.[15] In the spectrum of a 10 : 1 G1 : KTf_2N mixture, a third band is observed at 860 cm^{-1}, indicating the presence of G1 molecules that are coordinated to potassium cations. This shift to higher wavenumbers is significantly smaller than for the case of G1–NaFSI mixtures (866 cm^{-1}), probably because the charge density of K^+ cations is lower than that of Na^+ cations, and therefore the interactions with the G1 solvent are weaker.[15] The two bands that are characteristic of free G1 molecules are also still present, since, at this ratio, G1 is present in a large excess compared to KTf_2N. As the concentration of KTf_2N in
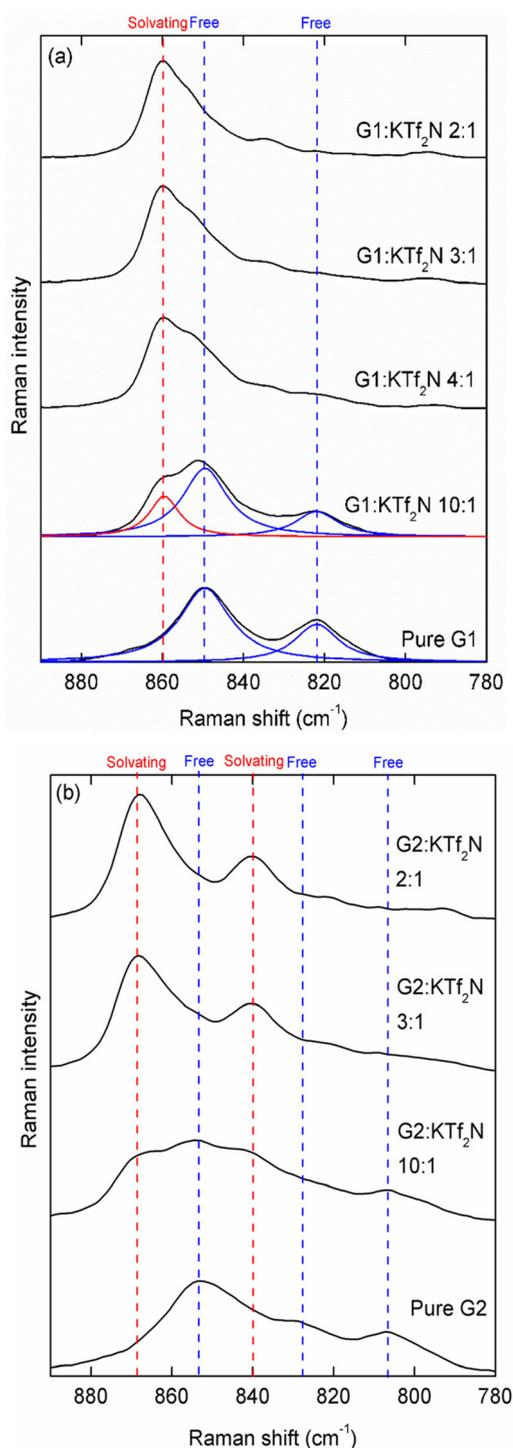

Fig. 4 Concentration dependence of the Raman spectra in the 780–890 cm^{-1} range for (a) G1–KTf_2N and (b) G2–KTf_2N mixtures. The Raman spectra of pure G1 and G2 are also included in the respective figures. The blue and red curves are peak fits produced by the deconvolution of the multipeaks, where the blue curves are fitted to bands characteristic of free glymes and the red curves to bands characteristic of solvating glymes.

the binary mixtures is increased, the band at 860 cm^{-1} becomes more intense, whereas the bands at 850 and 822 cm^{-1} become less intense, which indicates that the amount of free G1 molecules in the mixtures decreases. Generally speaking, with HCEs and SILs, the bands at 850 and 822 cm^{-1} should completely disappear, indicating that almost no free G1 is present in the mixtures and practically all the available G1 is coordinated. However, judging from the large shoulder on the 860 cm^{-1} band, this is not the case here. This means that even at a G1 : KTf$_2$N ratio of 2 : 1 there is still some uncoordinated G1 present, which is surprising and might be a consequence of the exceptionally weak G1–K$^+$ interactions and the poor chelate effect of G1. Besides the intense band at 860 cm^{-1}, a second less intense band at approx. 835 cm^{-1} is also observed. This can probably also be attributed to co-ordinated G1 molecules.

The Raman spectrum of pure diglyme is significantly more complex than that of monoglyme and it was not possible to produce a satisfactory multipeak fit in the 780–890 cm^{-1} region. According to Johansson *et al.*, the Raman spectrum of liquid diglyme is a combination of the individual spectra of a large number of different conformers that are in equilibrium with each other.[50] Thus, deconvolution of this multipeak in only three bands would be a very simplified representation. However, three bands can be distinguished in the raw Raman spectrum at approx. 807, 828, and 852 cm^{-1}, where the bands at 807 and 852 cm^{-1} correspond to the *trans* and *gauche* conformations of the C–C bond in diglyme, respectively. The band at 807 cm^{-1} corresponds to the coupled $r(CH_2)/tw(CH_2)$ modes, and the band at 852 cm^{-1} corresponds to the coupled $r(CH_2)/\nu(COC)$ modes of a free G2 molecule and both can be used as a fingerprint mode for solvation studies. In the spectrum of a 10 : 1 G2–KTf$_2$N mixture, two new bands appear at 841 and 868 cm^{-1} due to the coordination of G2 molecules to K$^+$ cations. Similarly to the G1–KTf$_2$N mixtures, these bands become more intense as the KTf$_2$N concentration increases, whereas the bands characteristic of free G2 become less intense. For the 2 : 1 G2–KTf$_2$N mixture, only a slight shoulder can be observed on the 868 cm^{-1} band, indicating that almost all of the available G2 solvent molecules are coordinated to K$^+$ cations. Judging from this behavior and the larger shift of the coordinated G2 band (868 cm^{-1}) compared to the uncoordinated band (852 cm^{-1}), the solvation of K$^+$ cations in G2 is significantly stronger than in G1, which is expected according to the chelate effect. For the 3 : 1 mixture, the band at 852 cm^{-1} can still barely be observed; hence in the liquid state, there is still a significant amount of free G2 present. This will also become evident from the coordination study of the Tf$_2$N$^-$ anion (*vide infra*).

The concentration dependance of the Raman spectra of G3–KTf$_2$N mixtures in the 780–890 cm^{-1} range is largely analogous to G2–KTf$_2$N mixtures (Fig. S6). The multipeak produced by pure G3 consists of roughly three bands at approx. 807, 829 and 851 cm^{-1}. Upon solvation of K$^+$ cations, *i.e.* for the 10 : 1 G3–KTf$_2$N mixture, two new bands appear in the spectrum at approx. 840 and 868 cm^{-1}. Interestingly, for the 2 : 1 mixture,

i.e. the solid SSIP solvate complex [K(G3)$_2$][Tf$_2$N], the solvating band is shifted to even higher wavenumbers (872 cm^{-1}). This was also observed for the sodium-containing solid solvate complex [Na(G3)$_2$][FSI].[15] This indicates an even stronger glyme–K$^+$ interaction in the solid complex compared to the liquid solutions because the glyme chains are wrapped even more tightly around the K$^+$ cation. It should be noted that it was not possible to measure many other G3–KTf$_2$N mixtures because crystals of [K(G3)$_2$][Tf$_2$N] started to precipitate out, leading to inhomogeneous mixtures.

The concentration dependence of the Raman spectra of G4–KTf$_2$N mixtures in the 780–890 cm^{-1} range is again analogous (Fig. S7). The spectrum of pure G4 in this region consists of roughly three bands at approx. 807, 829 and 851 cm^{-1}. When KTf$_2$N is added, two new bands at approx. 835 and 866 cm^{-1} are observed, corresponding to solvating G4 molecules. In this case, the 866 cm^{-1} band is not shifted to higher wavenumbers in the solid solvate complex [K(G4)][Tf$_2$N], as was the case for [K(G3)$_2$][Tf$_2$N]. Interestingly, for the liquid 2 : 1 G4–KTf$_2$N mixture, *i.e.* the solvate complex [K(G4)$_2$][Tf$_2$N] (mp: 19 °C), there is still a noticeable band of free G4 present in the Raman spectrum. This would mean that, even though [K(G4)$_2$][Tf$_2$N] very likely has an SSIP structure in the solid state, upon melting, some of the G4 ligands are desolvated from the K$^+$ cations. This is supported by the TGA data of this complex (*vide supra*), which showed relatively poor thermal stability for [K(G4)$_2$][Tf$_2$N].

The second region of interest for solvation studies of glyme–KTf$_2$N binary mixtures is located in the 710–770 cm^{-1} range. Here, the S–N stretching modes (ν(SN)) of the Tf$_2$N$^-$ anion are located, which are sensitive to its coordination environment. For a free (non-coordinating) Tf$_2$N$^-$ anion, this band is located at approx. 740 cm^{-1}.[27] On the other hand, in pure crystalline KTf$_2$N, which has an AGG structure, this band is located at approx. 744 cm^{-1}.[51] This shift is rather small but this can again be possibly explained by the low Lewis acidity of the K$^+$ cation. Thus, these bands can be used as fingerprint modes to assess the degree of ion pairing (*i.e.* CIP and AGG formation) in glyme–KTf$_2$N binary mixtures. The concentration dependence of the Raman spectra for G1–KTf$_2$N, G2–KTf$_2$N, G3–KTf$_2$N, and G4–KTf$_2$N binary mixtures in the 690–770 cm^{-1} range is shown in Fig. 5.

For all four systems, a dependence is observed between the ν(SN) band and the KTf$_2$N concentration. Upon increasing the KTf$_2$N concentration, the ν(SN) band shifts increasingly towards the 744 cm^{-1} of pure crystalline KTf$_2$N, indicating formation of CIPs and AGGs in the mixtures. When the different glyme systems are compared to each other, a trend is observed. For the G1–KTf$_2$N series of mixtures, the ν(SN) band is already shifted significantly towards higher wavenumbers even at the 10 : 1 G1 : KTf$_2$N ratio, meaning that even under these relatively dilute conditions, CIPs and AGGs are already formed. For the G2–KTf$_2$N series of mixtures, this is also the case but to a lesser extent than for the G1 analogues. For the G3–KTf$_2$N and G4–KTf$_2$N series, the ν(SN) band is located at approx. 740 cm^{-1} at the 10 : 1 ratio, indicating that the KTf$_2$N
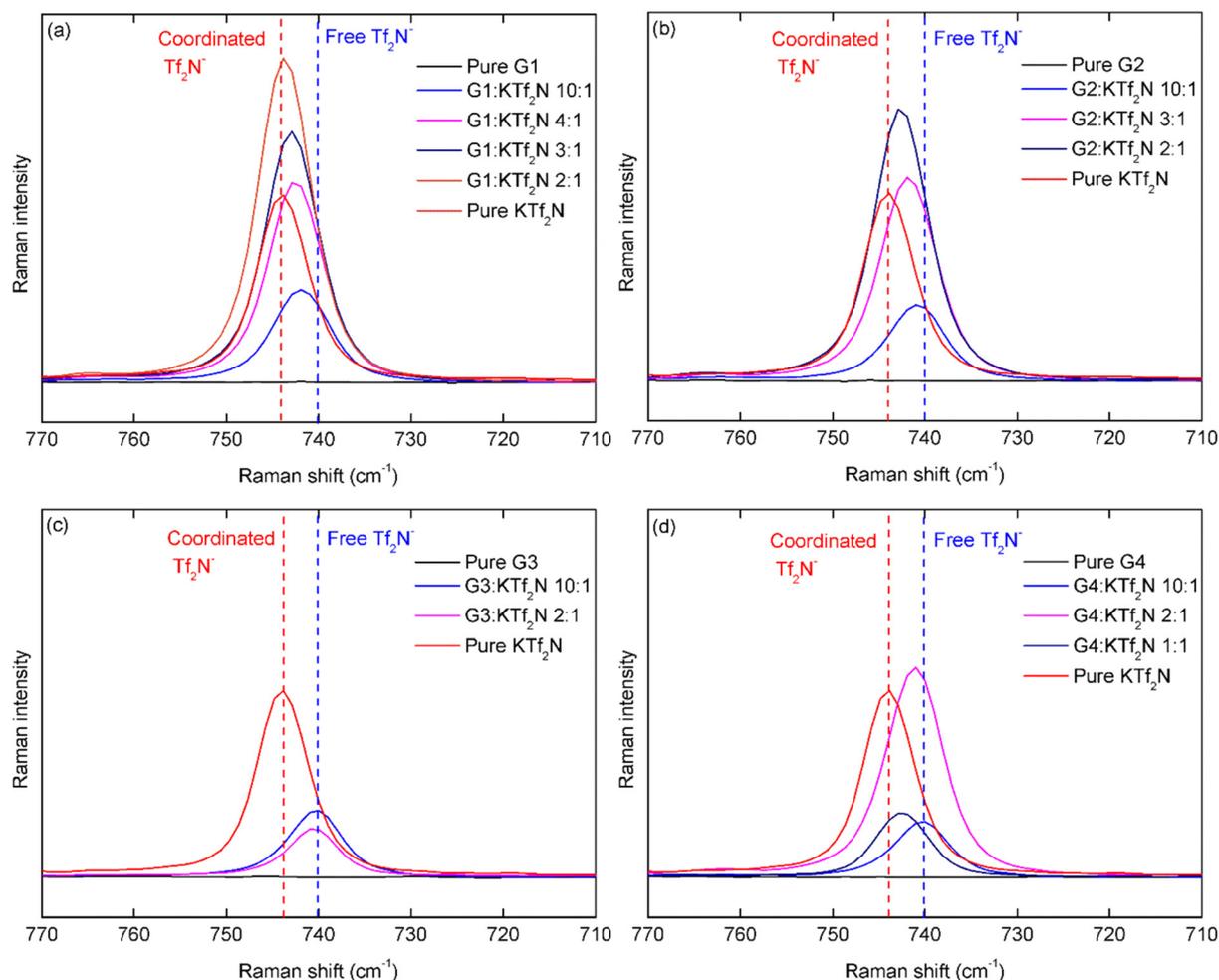
Fig. 5 Concentration dependence of the Raman spectra in the 690–770 cm^{-1} range for (a) G1–KTf$_2$N, (b) G2–KTf$_2$N, (c) G3–KTf$_2$N, and (d) G4–KTf$_2$N. G3–KTf$_2$N 3 : 1 was an inhomogeneous mixture and was omitted from the plot.

salt is fully dissociated into SSIPs at this concentration. For the 2 : 1 G3 : KTf$_2$N mixture, *i.e.* the solid SSIP solvate complex [K(G3)$_2$][Tf$_2$N], this band is not shifted to higher wavenumbers, which confirms the SSIP solvate structure of this complex which was revealed by single crystal XRD (*vide supra*). On the other hand, for the liquid 2 : 1 G4 : KTf$_2$N mixture, *i.e.* the solvate complex [K(G4)$_2$][Tf$_2$N] (mp: 19 °C), the ν(SN) band is shifted compared to the 740 cm^{-1} line. This supports the cationic Raman spectra and TGA data that in the liquid state, the second G4 ligand is easily desolvated and is replaced by Tf$_2$N$^-$ anions, leading to CIP and AGG formation. For the solid solvate complex [K(G4)][Tf$_2$N], the band is noticeably shifted, so the solvate structure in the solid state is indeed probably a CIP or AGG type. This is expected since the five available ether oxygen atoms in G4 are not sufficient to fill the first coordination shell of K$^+$. Therefore, Tf$_2$N$^-$ anions have to fill in the open positions.

Molecular dynamics (MD) simulations were performed to investigate the cation's solvation sphere and further rationalize the experimental findings (Fig. 6). The simulated systems com-

prise Gn–KTf$_2$N mixtures with n = 1–4 at compositions of 4 : 1, 3 : 1, and 2 : 1. Radial distribution functions (RDFs) were calculated to gain insights into the cation's interactions with the different species in the system. For the ease of comparison with the solvent, the discussion of the cation's interaction with the anion will be limited to the anion's oxygen atoms. The RDFs for the anion's center of mass can be found in the SI (Fig. S8 and S9).

Fig. 7 shows the RDFs for the cation's interactions with the oxygen atoms of the Tf$_2$N$^-$ anion and the glyme solvent as well as the interaction with other cations in the respective 2 : 1 mixtures of G1–KTf$_2$N and G4–KTf$_2$N. The RDFs for the other simulated systems can be found in the SI (Fig. S8 and S9). Sharp peaks are observed in both systems for the cation's interaction with the oxygen atoms of the anion and solvent located at a distance of 282 pm, indicating an ordered first coordination shell. In G1, the first peaks for the anion and solvent are similar in height and width, whereas in G4, the anion's peak is reduced compared to that of the solvent, as the anion is replaced in the cation's first solvation shell. At larger
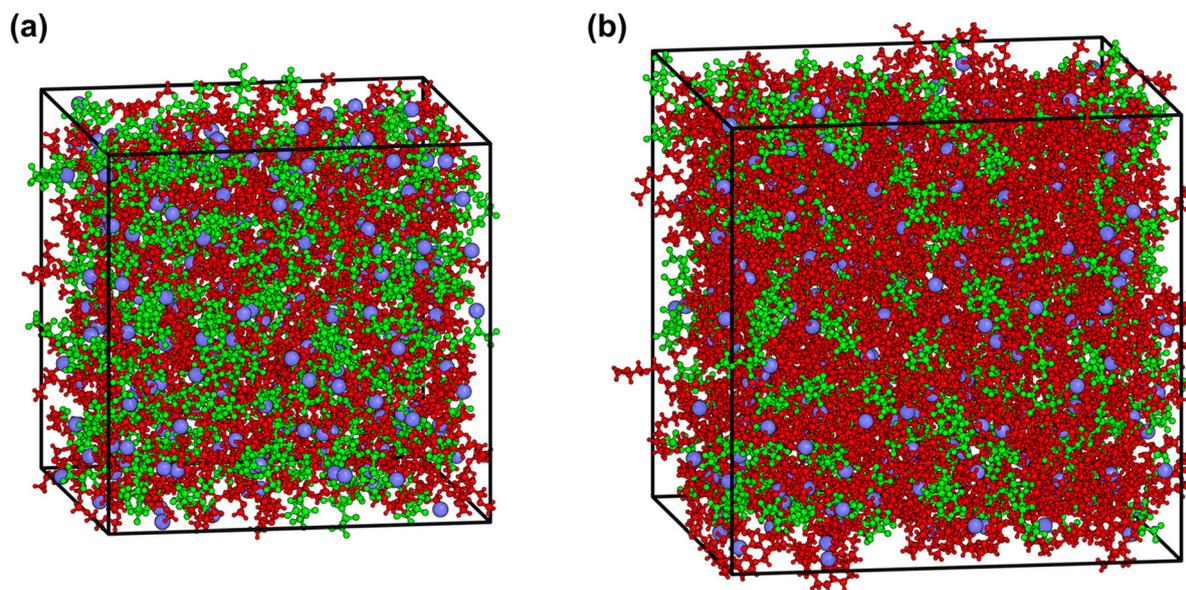
Fig. 6 Simulation boxes of the (a) G1–KTf$_2$N 2 : 1 system and (b) G4–KTf$_2$N 2 : 1 system. Red: G1/G4, blue: K$^+$, green: Tf$_2$N$^-$.
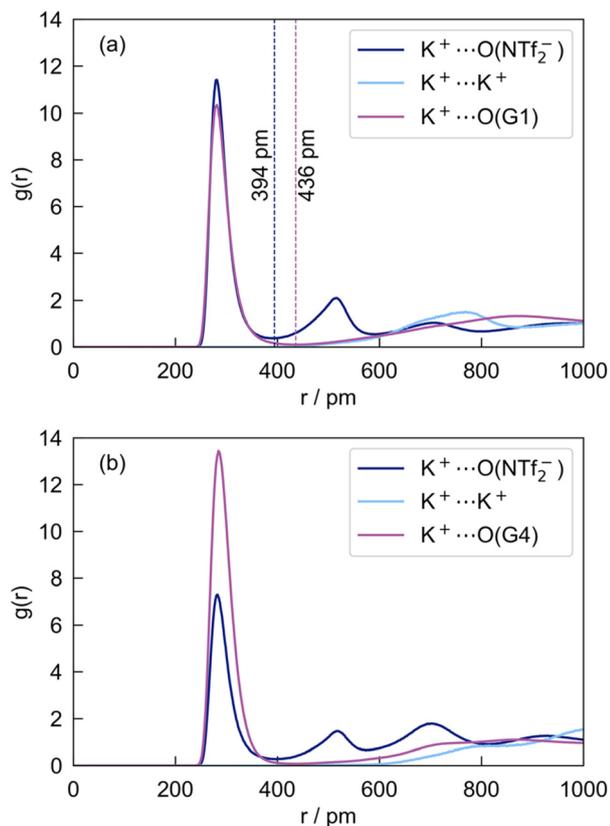

Fig. 7 Radial distribution functions (RDFs) of the K$^+$ cation interacting with other ions and the solvent in the 2 : 1 mixture of (a) G1–KTf$_2$N and (b) G4–KTf$_2$N.

distances, two smaller peaks are observed for the anion's oxygen atom located at 515 pm and 702 pm. These correspond to the non-coordinating oxygen atoms of a coordinating anion and an anion in the second solvation shell, respectively. In G4, the more distant peak gains intensity relative to the first two, indicating a shift from contact ion pairs to solvent separated ion pairs. No distinct peaks are observed in either system for the cation's interaction with the solvent's oxygen atoms at larger distances, indicating no ordered aggregation of solvent molecules around the cation beyond the first solvation shell. A small peak is observed in G1 for the cation's interaction with other cations located at 770 pm, whereas no peak is observed in G4. This may indicate a tendency for the formation of aggregates in G1 and their absence in G4.

It is evident that while the average coordination sphere of the cation changes with the solvent, the formation of CIPs remains significant even in the stronger chelating G4. To gain deeper insight into the composition of the cation's first solvation shell, neighbor count analyses were performed. An oxygen atom is considered part of the first solvation shell if it is within 394 pm for the anion and 436 pm for the solvent, which corresponds to the location of the first minimum in their respective RDFs (Fig. 7). By evaluating these conditions for every cation over the entire simulation trajectory, a histogram of the average number of cations coordinated by a given number of particles can be constructed. The obtained histograms are shown in Fig. 8. In agreement with the RDFs, it is evident that the formation of CIPs remains significant in all systems regardless of composition. In G1, the amount of cations with no direct contact to an anion's oxygen is <2% for all compositions. The number of fully solvated cations increases with both the glyme length and the amount of solvent, from 19% in G2–KTf$_2$N 4 : 1 to 54% in G3–KTf$_2$N 4 : 1
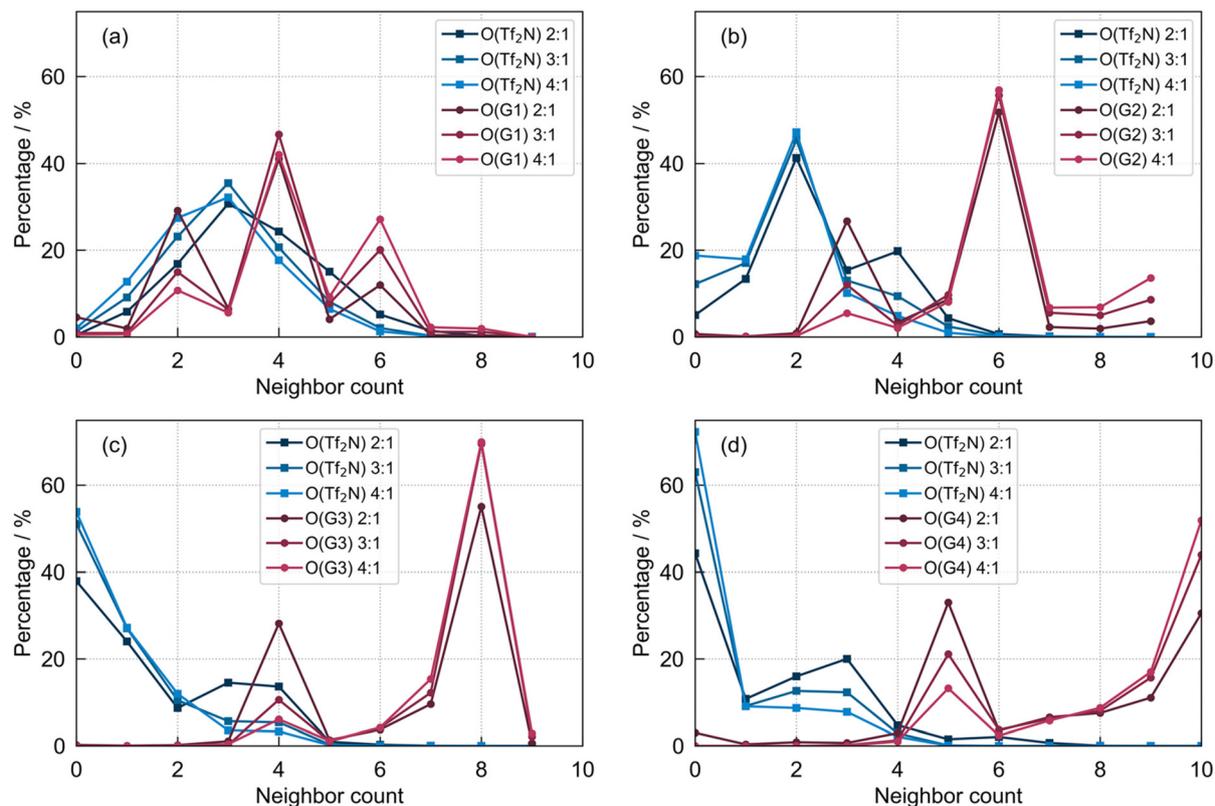
Fig. 8 Neighbor count histogram for the cation's first solvation shell in (a) G1, (b) G2, (c) G3, and (d) G4. Lines are meant to guide the eye.

and 72% in G4–KTf$_2$N 4 : 1. The solvent histograms show distinct peaks at neighbor counts corresponding to integer multiples of the number of oxygen atoms per solvent molecule, indicative of the chelate effect causing the solvent molecules to fully coordinate to a cation rather than being partly involved in its first solvation shell. Consequently, the most populated solvent oxygen neighbor counts increase with glyme length, from 4 in G1 to 6, 8, and 10 in G2, G3, and G4, respectively. In G1 and G2, a small but significant number of cations have neighbor counts of 6 or 9, respectively, corresponding to coordination by three solvent molecules. In contrast, coordination by more than two solvent molecules is not observed in G3 and G4. Counting both the anion and solvent oxygen atoms, the total coordination number rises with both the glyme length and the amount of solvent from an average of 6.9 in G1–KTf$_2$N 2 : 1 to 7.2 in G1–KTf$_2$N 4 : 1 and 8.6 in G4–KTf$_2$N 2 : 1.

These trends are broadly consistent with the experimentally observed Raman shifts. The ν(SN) Raman band probes the local coordination environment of the Tf$_2$N$^-$ anion. Therefore, to allow a direct comparison between the computationally obtained ion pair population and Raman trends, we calculated the fraction of anions bound in AGG structures (see Tables S7–S14), defined as Tf$_2$N$^-$ coordinated by two or more cations. At the most dilute simulated composition (4 : 1), this fraction decreases sharply with glyme length from 70% in G1 to 27% in G2, 7% in G3, and 3% in G4. This is in good agreement with

the experimentally observed persistence of the ν(SN) upshift in G1 but not in G3 and G4. Upon increasing the salt concentration from 4 : 1 to 2 : 1, the amount of anions bound in AGG structures increases in all systems (*e.g.*, from 3% to 26% in G4), consistent with the ν(SN) shift toward the solid KTf$_2$N limit. A plot of the Raman ν(SN) peak position against the MD-derived AGG fraction (Fig. S10) shows a strong qualitative correlation.

Fig. 9(a) shows the cation binding energy as obtained from DFT calculations as a function of the number of coordinating glyme molecules in the absence of the anion. The binding energy of a single glyme molecule coordinating the cation increases from G1 to G4. Each additional glyme molecule has a diminishing contribution to the total binding energy until the cation's coordination sphere is saturated and the contribution of further molecules drops to <50 kJ mol^{-1}. As the number of oxygen atoms per coordinating glyme molecule increases, saturation is reached after fewer molecules. Following the series G1, G2, and G3, the cation can fit up to four, three, or two glyme molecules in its coordination shell, respectively. Remarkably, two molecules of G4 may fully coordinate the cation. The binding energy of the saturated cation lies in the range of 430 kJ mol^{-1} to 480 kJ mol^{-1} which is similar to the isolated KTf$_2$N ion pair's binding energy of 441 kJ mol^{-1}. Fig. 9(b) shows the binding energy in the presence of the anion. Similar trends to that for the anion-free clusters are observed. However, due to the steric hindrance by
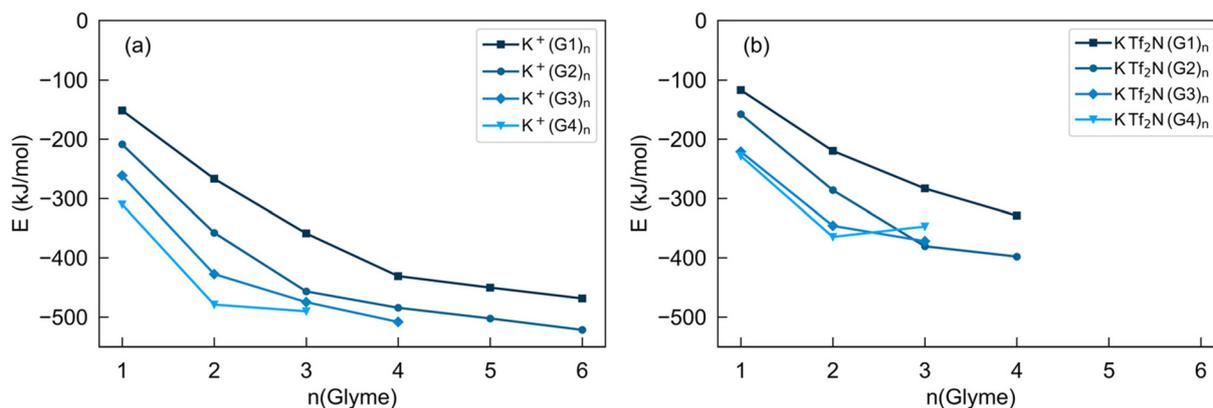
Fig. 9 (a) Binding energy $E_b(n) = E(K^+(Glyme)_n) - E(K^+) - E((Glyme)_n)$ of the K^+ cation coordinated by a number of n glyme molecules. (b) Binding energy $E_b(n) = E(KTf_2N(Glyme)_n) - E(KTf_2N) - E((Glyme)_n)$ of the KTf_2N ion pair coordinated by a number of n glyme molecules.

the anion, the glyme molecules may not be able to fully coordinate the cation and their binding energy is significantly reduced. This effect increases with the number of glyme molecules and their size.

Electrochemical stabilities were calculated for the different glymes and their complexes formed with the cation in the presence and absence of the anion. The obtained potentials U_{red} and U_{ox} for reduction and oxidation of various species and complexes are listed in Table 2. For the glymes in their isolated form, the U_{red} and U_{ox} shift towards more positive and more negative values, respectively, as the glyme length increases, implying a smaller electrochemical stability window for G4 compared to G1. When forming a complex with the K^+ cation, the reduction and oxidation potentials shift towards more positive values. Remarkably, compared to the isolated glymes, the trend of U_{red} is reversed as it shifts slightly towards more negative values with increasing glyme length. This trend also persists in the presence of the anion. The addition of the anion shifts all potentials towards more negative values.

Notably, compared to the isolated ion pair, U_{red} is reduced for the glyme complexes. When comparing the saturated complexes, as established from the previous DFT analysis, U_{red} is similar for all glymes, whereas no clear trend is observed for U_{ox} which fluctuates with increasing glyme length.

To summarize: the complexes with the general formula [K(L)$_n$][Tf$_2$N] (L = G1, G2, G3, or G4; n = 2, 3 or 4) are low-melting solvate complexes between an ion (K^+) and ligands (glymes) in a certain stoichiometric ratio, thereby satisfying criteria 1, 3 and 4 for SILs, as proposed by Mandai *et al.*[49] However, because of the weaker K^+–glyme interactions, significant ion pairing occurs and the thermal stability is rather poor, not meeting criteria 2 and 5. This is especially the case for the complexes with shorter glyme ligands (G1 and G2). Therefore, [K(G1)$_2$][Tf$_2$N] and [K(G2)$_2$][Tf$_2$N] are classified as "poor" SILs whereas [K(G3)$_2$][Tf$_2$N] and [K(G4)$_2$][Tf$_2$N] are more akin to "true" SILs, which is expected based on the stronger chelating properties of the longer glyme ligands.

Cycling of [K(G1)$_2$][Tf$_2$N] and [K(G2)$_2$][Tf$_2$N] on organic cathodes

To be useful as a battery electrolyte, the electrochemical window of the electrolyte should be wider than the operating potential window of the battery. Therefore, the electrochemical window of [K(G1)$_2$][Tf$_2$N] and [K(G2)$_2$][Tf$_2$N] was determined using cyclic voltammetry with a platinum working electrode (Fig. 10). These two HCEs were selected for further electrochemical studies since they exhibited behavior closest to that of SILs, albeit "poor" SILs (*vide supra*), while also having an acceptable ionic conductivity. [K(G3)$_2$][Tf$_2$N] and [K(G4)][Tf$_2$N] are solids at room temperature and [K(G4)$_2$][Tf$_2$N] has a rather low ionic conductivity, so they were omitted from testing. Any other mixture has significant amounts of free glymes present so they cannot be categorized as HCEs or SILs. For the remainder of this discussion, the general term HCEs will be used to refer to the poor SILs [K(G1)$_2$][Tf$_2$N] and [K(G2)$_2$][Tf$_2$N].

For both HCEs, the cathodic limit corresponds to the deposition of potassium metal which occurs at a potential of −3.3 V

Table 2 Calculated reduction (U_{red}) and oxidation (U_{ox}) potentials for the cation and its complexes with various species

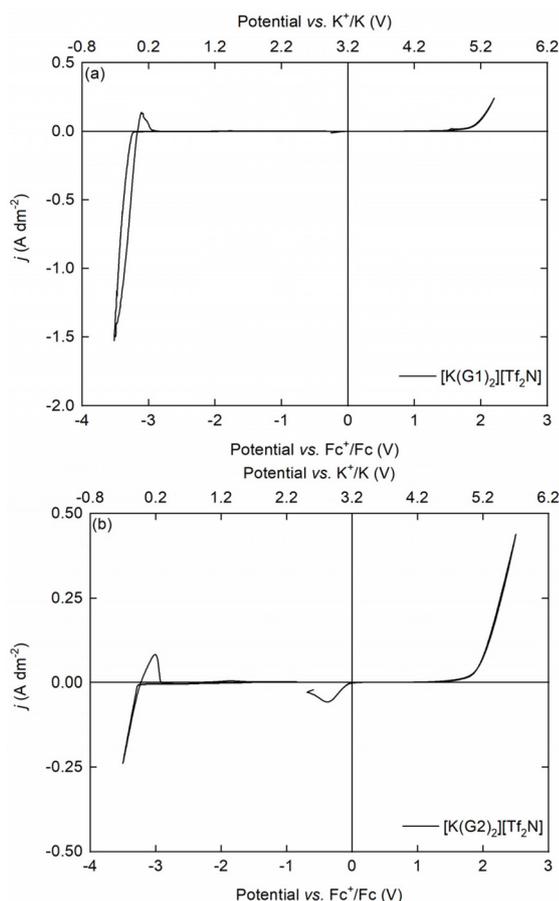| Complex/species	U_{red} (V)	U_{ox} (V)
[Tf$_2$N]$^-$	−0.4	5.3
KTf$_2$N	−0.5	6.3
G1	−2.5	5.8
G2	−2.4	5.7
G3	−2.4	5.7
G4	−2.4	5.7
[K(G1)]$^+$	0.0	6.3
[K(G2)]$^+$	−0.2	6.7
[K(G3)]$^+$	−0.4	6.6
[K(G4)]$^+$	−0.5	6.5
[K(G1)][Tf$_2$N]	−0.7	5.7
[K(G2)][Tf$_2$N]	−0.9	5.7
[K(G3)][Tf$_2$N]	−1.0	5.6
[K(G4)][Tf$_2$N]	−1.0	5.2
[K(G1)$_4$]$^+$	−1.0	6.2
[K(G2)$_3$]$^+$	−1.0	5.9
[K(G3)$_2$]$^+$	−1.0	6.2
[K(G4)$_2$]$^+$	−1.0	5.9

Fig. 10 Cyclic voltammograms of (a) [K(G1)$_2$][Tf$_2$N] and (b) [K(G2)$_2$][Tf$_2$N], measured on a platinum working electrode with a scan rate of 10 mV s^{-1}. The counter electrode was platinum and the reference electrode was a platinum wire submerged in a solution of ferrocene (Fc) and ferrocenium hexafluorophosphate (FcPF$_6$) (5 mmol L^{-1} each) in [BMP][Tf$_2$N], contained inside a fritted glass tube (referred to as Fc$^+$/Fc). The threshold for determination of the electrochemical window was 1% of the maximum potassium plating current density.

vs. Fc$^+$/Fc, which should correspond to approx. −0.1 V *vs.* K$^+$/K, considering that the electrodeposition of alkali metals is usually characterized by a small overpotential. This is evidenced by the sudden negative increase in current density at this potential in the forward cathodic scan, and the corresponding stripping peak in the backward scan. Judging from the size of the stripping peak in relation to the potassium electrodeposition current density, the deposition/stripping of potassium metal is clearly not very reversible. The observed coulombic efficiency for potassium deposition/stripping was 4% for [K(G1)$_2$][Tf$_2$N] and 28% for [K(G2)$_2$][Tf$_2$N]. Due to the high reactivity of potassium metal and its tendency to deposit dendritically at these high current densities, most of the deposit reacts with electrolyte components or gets lost from the working electrode as "dead" potassium. The anodic limit of the HCEs is around +1.7 V *vs.* Fc$^+$/Fc (or +4.9 V *vs.* K$^+$/K) and corresponds to the decomposition of the ligands. Overall, all of the HCEs have an electrochemical window of approximately 5.0 V.

Since the electrodes used in the cycling experiments can also have a significant influence on the limiting potentials of the electrochemical window, the voltage range was chosen well within the determined boundaries (−1.0 V to +1.0 V *vs.* activated carbon (AC), which is about +2.0 V to +4.0 V *vs.* K$^+$/K). For the galvanostatic cycling experiments, because of the high reactivity of potassium metal with the electrolyte, activated capacitive carbon (AC) was chosen as the counter/reference electrode instead of potassium metal. For the cathode (working electrode) material, the organic coordination polymer K$_2$–Co–benzene-1,2,4,5-tetra-methylsulfonamide (K$_2$–Co–PTtSA) was chosen, which is reported elsewhere.[32] K$_2$–Co–PTtSA is, to date, the first and only reported cathode material synthesized directly in its reduced state, meaning that it is intrinsically potassium-containing. As such, it can operate as a cathode in a manner analogous to conventional lithium-ion battery cathodes. However, this system also presents several limitations. Although its electrical conductivity is relatively high for an organic battery material, it remains limited (approx. 10^{-7} S cm^{-1}). Consequently, a large fraction of conductive carbon additives (typically 20–10 wt%) is required in the electrode composite, significantly reducing the practical capacity of the cathode. In addition, as a coordination polymer, the interactions between the organic ligand and the inorganic metal centers, while strong, are generally weaker than those found in fully inorganic materials. As a result, the choice of electrolyte becomes critical, as it directly governs the solubility of the coordination polymer. Excessive solubility in the electrolyte leads to rapid capacity fading and severely compromises the cycle life of the battery. Therefore, careful electrolyte design is essential to ensure sufficient ionic conductivity while simultaneously mitigating cathode dissolution, thereby enabling stable long-term electrochemical performance. In this regard, [K(G1)$_2$][Tf$_2$N] and [K(G2)$_2$][Tf$_2$N] are promising electrolytes to pair with K$_2$–Co–PTtSA because nearly all the glyme molecules are coordinated to K$^+$ cations and are therefore less available to dissolve the cathode material, potentially improving the capacity retention. Besides [K(G1)$_2$][Tf$_2$N] and [K(G2)$_2$][Tf$_2$N], an electrolyte consisting of 1 mol L^{-1} KPF$_6$ in ethylene carbonate (EC) : propylene carbonate (PC) was chosen as a standard reference electrolyte to compare the HCEs to. The galvanostatic cycling results for 200 cycles at a cycling rate of C/10 are depicted in Fig. 11.

Upon comparing the three different electrolyte systems, some significant differences can be observed (Fig. 11a). In the first cycle, the specific discharge capacity is almost equal for all three electrolytes at approx. 77 mAh g^{-1}. However, for the 1 mol L^{-1} KPF$_6$ in the EC : PC electrolyte, a fast capacity fade is observed over 200 cycles to a final specific discharge capacity of approx. 15 mAh g^{-1}. For the [K(G1)$_2$][Tf$_2$N] electrolyte, capacity fading is also observed but at a much slower rate, with a final specific discharge capacity of approx. 30 mAh g^{-1} after 200 cycles. On the other hand, the specific discharge capacity of the cell with the [K(G2)$_2$][Tf$_2$N] electrolyte even slightly increases in the first ten cycles, and then remains remarkably stable to a final value of approx. 70 mAh g^{-1}. In
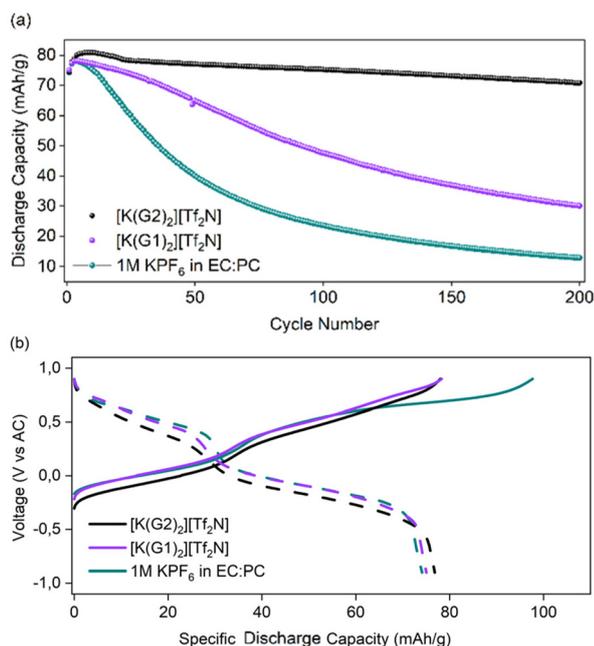
Fig. 11 Cycling performance of K$_2$–Co–PTtSA cathodes in [K(G1)$_2$][Tf$_2$N], [K(G2)$_2$][Tf$_2$N], and 1 mol L^{-1} KPF$_6$ in EC : PC at a cycling rate of C/10. (a) Discharge capacity vs. cycle number over 200 cycles and (b) first cycle charge/discharge profiles for each electrolyte.

the charge/discharge profiles, it can be observed that although the discharge capacity in the three electrolytes is almost equal, the charge capacity is in fact significantly higher for the reference electrolyte, 1 mol L^{-1} KPF$_6$ in EC : PC (Fig. 11b). Thus, the coulombic efficiency is lower for 1 mol L^{-1} KPF$_6$ in EC : PC (approx. 93%) compared to [K(G1)$_2$][Tf$_2$N] and [K(G2)$_2$][Tf$_2$N] (almost 100%). As mentioned above, this behavior could be possibly explained by a lower solubility of the cathode active material in [K(G1)$_2$][Tf$_2$N] and [K(G2)$_2$][Tf$_2$N] compared to the EC : PC electrolyte, or by a higher degree of irreversible side reactions in the latter electrolyte. To complement this discussion, a qualitative solubility test was performed by dispersing 10 mg of pristine K$_2$–Co–PTtSA in 2 mL of the corresponding electrolytes, followed by sonication for 10 minutes. After 24 h, the suspensions were filtered, and the resulting filtrates are shown in Fig. S11. As observed, the EC : PC-based electrolyte exhibits a markedly darker coloration compared to [K(G1)$_2$][Tf$_2$N], which itself is darker than [K(G2)$_2$][Tf$_2$N]. The pink coloration, characteristic of the dissolved PTtSA ligand, indicates a higher degree of coordination polymer dissolution in the EC : PC-based electrolyte, followed by [K(G1)$_2$][Tf$_2$N], and the lowest solubility in [K(G2)$_2$][Tf$_2$N]. This qualitative trend in solubility correlates well with the electrochemical results and provides a plausible explanation for the superior capacity retention observed with [K(G2)$_2$][Tf$_2$N], compared to [K(G1)$_2$][Tf$_2$N] and the EC : PC-based standard electrolyte. Secondly, as reported by Hosaka et al., G2-based HCEs exhibit a significantly higher oxidative stability than G1-based HCEs, which also contributes to the higher observed stability of [K(G2)$_2$][Tf$_2$N].[25]

Secondly, the rate performance of K$_2$–Co–PTtSA was investigated in the three electrolyte systems (Fig. 12).

When comparing the rate performance of K$_2$–Co–PTtSA cathodes in the three electrolytes, some significant differences can be observed here as well (Fig. 12a). For 1 mol L^{-1} KPF$_6$ in EC : PC, the rate performance is relatively good, as the achieved specific discharge capacity remains around 81 mAh g^{-1} up to a cycling rate of 2C. Only at 5C and 10C, the specific discharge capacity is slightly decreased. However, for [K(G2)$_2$][Tf$_2$N] and especially [K(G1)$_2$][Tf$_2$N], the rate performance is significantly worse, as the specific discharge capacity already decreases at a cycling rate of C/5. At 10C, the achieved specific discharge capacity is only approx. 25 mAh g^{-1} for [K(G2)$_2$][Tf$_2$N] and approx. 15 mAh g^{-1} for [K(G1)$_2$][Tf$_2$N]. This behavior can possibly be explained by the higher viscosity and lower ionic conductivity of the HCEs compared to the reference electrolyte. Furthermore, these electrolyte properties are also strongly linked to other kinetic limitations, including charge-transfer resistance at the electrode–electrolyte interface and mass transport within the porous electrode. As the electrolyte ionic conductivity decreases and viscosity increases, ion mobility is reduced, leading to the development of steeper concentration gradients under high current densities. This not only slows interfacial charge-transfer kinetics, but also imposes severe mass-transport limitations, particularly within the electrolyte-filled pores of the composite electrode. In such conditions, the replenishment of K$^+$ cations at the active material surface
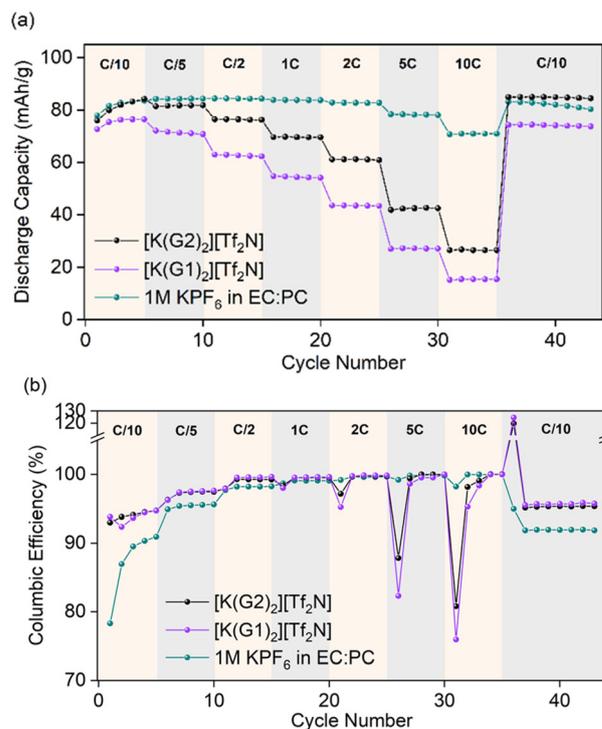

Fig. 12 Rate performance of K$_2$–Co–PTtSA cathodes in [K(G1)$_2$][Tf$_2$N], [K(G2)$_2$][Tf$_2$N], and 1 mol L^{-1} KPF$_6$ in EC : PC at cycling rates ranging from C/10 to 10C. (a) Specific discharge capacity vs. cycle number and (b) coulombic efficiency vs. cycle number.

becomes rate-limiting, resulting in increased polarization and diminished rate capability. However, even though [K(G1)$_2$][Tf$_2$N] is less viscous and more conductive than [K(G2)$_2$][Tf$_2$N], its rate performance is actually worse, so this cannot be the only reason. Another factor that can contribute to charge-transfer limitations is the possible formation of a cathode–electrolyte interface (CEI) through side reactions of the charged cathode surface and electrolyte components. However, analysis of the CEI on this novel organic cathode material is very challenging and is outside the scope of this work. Looking at the coulombic efficiency, the two HCEs consistently achieve higher values than the reference electrolyte (Fig. 12b). Therefore, it can be concluded that the HCEs outperform the reference electrolyte in terms of long-term stability but are outperformed in terms of rate performance. The rate performance of the HCEs can be possibly improved by using them to prepare localized high concentration electrolytes (LHCEs), which would increase the ionic conductivity significantly but keep the unique solvation structures of HCEs.[26] However, this was outside the scope of the present work.

Conclusion

Complexes with the general formula [K(L)$_n$][Tf$_2$N] (L = G1, G2, G3, or G4; n = 2, 3 or 4) were prepared and characterized. These complexes are classified as HCEs owing to their high concentration of KTf$_2$N. They were subsequently systematically investigated to see if they could also be classified as SILs, according to the criteria proposed by Mandai *et al.* Many of the HCEs are liquids at room temperature and have a reasonably low viscosity, making them potential candidates for use as electrolytes in KIBs. Their volatility, although reduced compared to pure glymes, was still high, especially for the G1 and G2 HCEs. The solvation structure of the HCEs was extensively studied using single crystal XRD and Raman spectroscopy, supported by molecular dynamics studies and DFT calculations. This revealed that a significant amount of ion pairing and aggregate formation occurred for all the tested HCEs. For the G1 and G2 HCEs, this even occurred at relatively dilute concentrations. Therefore, the HCEs must be classified as "poor" SILs, since they lack some of the proposed criteria for "true" SILs. Despite this, the electrolytes [K(G1)$_2$][Tf$_2$N] and [K(G2)$_2$][Tf$_2$N] still exhibited acceptable conductivity, so they were selected for a proof-of-concept galvanostatic cycling study on the organic cathode material K$_2$–Co–PTtSA. These two HCEs showed improved long-term cycling stability (less capacity fading and higher coulombic efficiency) compared to a standard reference electrolyte consisting of 1 mol L^{-1} KPF$_6$ in EC : PC, but a worse rate performance due to the high viscosity.

Conflicts of interest

There are no conflicts to declare

Data availability

The data supporting this article have been included as part of the supplementary information (SI). Supplementary information: conductivity, viscosity, density and potassium concentration of glyme–KTf$_2$N electrolytes (Tables S1–S4), crystallographic data of [K(G3)$_2$][Tf$_2$N] (Table S5), molecular dynamics parameters of various glyme–KTf$_2$N systems (Table S6), population analysis of AGG structures in various glyme–KTf$_2$N systems (Tables S7–S14), dynamic TGA curves of glyme–KTf$_2$N complexes (Fig. S1–S4), close-up of the crystal structure of [K(G3)$_2$][Tf$_2$N] (Fig. S5), Raman spectra of G3–KTf$_2$N and G4–KTf$_2$N systems in the 890–780 cm^{-1} range (Fig. S6–S7), RDFs of K$^+$ interacting with different moieties in glyme–KTf$_2$N systems at different ratios (Fig. S8–S9), correlation graph of the Raman ν(SN) peak position with the fraction of Tf$_2$N$^-$ anions bound in AGG structures as obtained from MD (Fig. S10), and solubility test of pure K$_2$–Co–PTtSA in the different used electrolytes (Fig. S11). See DOI: https://doi.org/10.1039/d5dt02781k.

CCDC 2488110 contains the supplementary crystallographic data for this paper.[52]

References

1 N. Yabuuchi, K. Kubota, M. Dahbi and S. Komaba, *Chem. Rev.*, 2014, **114**, 11636–11682, DOI: 10.1021/cr500192f.
2 J. Muldoon, C. B. Bucur and T. Gregory, *Chem. Rev.*, 2014, **114**, 11683–11720, DOI: 10.1021/cr500049y.
3 T. Hosaka, K. Kubota, A. S. Hameed and S. Komaba, *Chem. Rev.*, 2020, **120**, 6358–6466, DOI: 10.1021/acs.chemrev.9b00463.
4 J. Sun, Y. Du, Y. Liu, D. Yan, X. Li, D. H. Kim, Z. Lin and X. Zhou, *Chem. Soc. Rev.*, 2025, **54**, 2543–2594, DOI: 10.1039/d4cs00845f.
5 S. Komaba, T. Hasegawa, M. Dahbi and K. Kubota, *Electrochem. Commun.*, 2015, **60**, 172–175, DOI: 10.1016/j.elecom.2015.09.002.
6 K. Kubota, M. Dahbi, T. Hosaka, S. Kumakura and S. Komaba, *Chem. Rec.*, 2018, **18**, 459–479, DOI: 10.1002/tcr.201700057.
7 A. Eftekhari, *J. Power Sources*, 2004, **126**, 221–228, DOI: 10.1016/j.jpowsour.2003.08.007.
8 M. Okoshi, Y. Yamada, S. Komaba, A. Yamada and H. Nakai, *J. Electrochem. Soc.*, 2017, **164**, A54–A60, DOI: 10.1149/2.0211702jes.
9 M. Morita, T. Shibata, N. Yoshimoto and M. Ishikawa, *Electrochim. Acta*, 2002, **47**, 2787–2793, DOI: 10.1016/S0013-4686(02)00164-0.

10 X. Bie, K. Kubota, T. Hosaka, K. Chihara and S. Komaba, *J. Mater. Chem. A*, 2017, **5**, 4325–4330, DOI: 10.1039/c7ta00220c.

11 C. Zhang, Y. Xu, M. Zhou, L. Liang, H. Dong, M. Wu, Y. Yang and Y. Lei, *Adv. Funct. Mater.*, 2017, **27**, 1604307, DOI: 10.1002/adfm.201604307.

12 J. Liao, Q. Hu, Y. Yu, H. Wang, Z. Tang, Z. Wen and C. Chen, *J. Mater. Chem. A*, 2017, **5**, 19017–19024, DOI: 10.1039/C7TA05460B.

13 Z. Jian, W. Luo and X. Ji, *J. Am. Chem. Soc.*, 2015, **137**, 11566–11569, DOI: 10.1021/jacs.5b06809.

14 G. Vanhoutte, N. R. Brooks, S. Schaltin, B. Opperdoes, L. van Meervelt, J.-P. Locquet, P. M. Vereecken, J. Fransaer and K. Binnemans, *J. Phys. Chem. C*, 2014, **118**, 20152–20162, DOI: 10.1021/jp505479x.

15 P. Geysens, V. S. Rangasamy, S. Thayumanasundaram, K. Robeyns, L. van Meervelt, J.-P. Locquet, J. Fransaer and K. Binnemans, *J. Phys. Chem. B*, 2018, **122**, 275–289, DOI: 10.1021/acs.jpcb.7b10158.

16 P. Geysens, J. Fransaer and K. Binnemans, *RSC Adv.*, 2020, **10**, 42021–42029, DOI: 10.1039/d0ra08187f.

17 Y. Yamada and A. Yamada, *J. Electrochem. Soc.*, 2015, **162**, A2406–A2423, DOI: 10.1149/2.0041514jes.

18 Y. Yamada, K. Furukawa, K. Sodeyama, K. Kikuchi, M. Yaegashi, Y. Tateyama and A. Yamada, *J. Am. Chem. Soc.*, 2014, **136**, 5039–5046, DOI: 10.1021/ja412807w.

19 Y. Yamada, K. Usui, C. H. Chiang, K. Kikuchi, K. Furukawa and A. Yamada, *ACS Appl. Mater. Interfaces*, 2014, **6**, 10892–10899, DOI: 10.1021/am5001163.

20 M. Nie, D. P. Abraham, D. M. Seo, Y. Chen, A. Bose and B. L. Lucht, *J. Phys. Chem. C*, 2013, **117**, 25381–25389, DOI: 10.1021/jp409765w.

21 Q. Feng, J. Jiang, S. Li, G. Zhou, X. Kong, Y. Chen, Q. Zhuang and Z. Ju, *Small*, 2025, **21**, 2406506, DOI: 10.1002/smll.202406506.

22 Z. Yuan, J. Liao, L. Song, A. Chen, J. Su, J. Wang and X. Zhou, *Angew. Chem., Int. Ed.*, 2025, **64**, e202415923, DOI: 10.1002/anie.202415923.

23 N. Xiao, W. D. McCulloch and Y. Wu, *J. Am. Chem. Soc.*, 2017, **139**, 9475–9478, DOI: 10.1021/jacs.7b04945.

24 T. Hosaka, K. Kubota, H. Kojima and S. Komaba, *Chem. Commun.*, 2018, **54**, 8387–8390, DOI: 10.1039/c8cc04433c.

25 T. Hosaka, T. Matsuyama, K. Kubota, R. Tatara and S. Komaba, *J. Mater. Chem. A*, 2020, **8**, 23766–23771, DOI: 10.1039/d0ta08851j.

26 W. Xu, H. Wang, Y. Gao, Y. Wie, H. Zhang, C. Gao, F. Kang and D. Zhai, *Energy Adv.*, 2022, **1**, 191–196, DOI: 10.1039/d2ya00015f.

27 T. Mandai, S. Tsuzuki, K. Ueno, K. Dokko and M. Watanabe, *Phys. Chem. Chem. Phys.*, 2015, **17**, 2838–2849, DOI: 10.1039/c4cp05017g.

28 G. Zeng, S. Xiong, Y. Qian, L. Ci and J. Feng, *J. Electrochem. Soc.*, 2019, **166**, A1217–A1222, DOI: 10.1149/2.1171906jes.

29 O. V. Dolomanov, L. J. Bourhis, R. J. Gildea, J. A. K. Howard and H. Puschmann, *J. Appl. Crystallogr.*, 2009, **42**, 339–341, DOI: 10.1107/S0021889808042726.

30 G. M. Sheldrick, *Acta Crystallogr., Sect. A:Found. Adv.*, 2015, **71**, 3–8, DOI: 10.1107/S2053273314026370.

31 G. M. Sheldrick, *Acta Crystallogr., Sect. C:Struct. Chem.*, 2015, **71**, 3–8, DOI: 10.1107/S2053273314026370.

32 J. Wang, X. Guo, P. Apostol, X. Liu, K. Robeyns, L. Gence, C. Morari, J.-F. Gohy and A. Vlad, *Energy Environ. Sci.*, 2022, **15**, 3923–3932, DOI: 10.1039/d2ee00566b.

33 A. P. Thompson, H. M. Aktulga, R. Berger, D. S. Bolintineanu, W. M. Brown, P. S. Crozier, P. J. in 't Veld, A. Kohlmeyer, S. G. Moore and T. D. Nguyen, *Comput. Phys. Commun.*, 2022, **271**, 108171, DOI: 10.1016/j.cpc.2021.108171.

34 W. L. Jorgensen, D. S. Maxwell and J. Tirado-Rives, *J. Am. Chem. Soc.*, 1996, **118**, 11225–11236, DOI: 10.1021/ja9621760.

35 K. P. Jensen and W. L. Jorgensen, *J. Chem. Theory Comput.*, 2006, **2**, 1499–1509, DOI: 10.1021/ct600252r.

36 J. E. Lennard-Jones, *Proc. Phys. Soc.*, 1931, **43**, 461, DOI: 10.1088/0959-5309/43/5/301.

37 L. Martínez, R. Andrade, E. G. Birgin and J. M. Martínez, *J. Comput. Chem.*, 2009, **30**, 2157–2164, DOI: 10.1002/jcc.21224.

38 S. Nosé, *J. Phys.: Condens. Matter*, 1990, **2**, SA115, DOI: 10.1088/0953-8984/2/S/013.

39 W. G. Hoover, H. A. Posch, B. L. Holian, M. J. Gillan, M. Mareschal and C. Massobrio, *Mol. Simul.*, 1987, **1**, 79–86, DOI: 10.1080/08927028708080932.

40 F. Neese, F. Wennmohs, U. Becker and C. Riplinger, *J. Chem. Phys.*, 2020, **152**, DOI: 10.1063/5.0004608.

41 S. Grimme, J. Antony, S. Ehrlich and H. Krieg, *J. Chem. Phys.*, 2010, **132**, DOI: 10.1063/1.3382344.

42 S. Grimme, S. Ehrlich and L. Goerigk, *J. Comput. Chem.*, 2011, **32**, 1456–1465, DOI: 10.1002/jcc.21759.

43 H. Kruse and S. Grimme, *J. Chem. Phys.*, 2012, **136**, DOI: 10.1063/1.3700154.

44 O. Borodin, W. Behl and T. R. Jow, *J. Phys. Chem. C*, 2013, **117**, 8661–8682, DOI: 10.1021/jp400527c.

45 J. Wang and Y. Wang, *J. Phys. Chem. B*, 2024, **128**, 1943–1952, DOI: 10.1021/acs.jpcb.3c08127.

46 V. Barone and M. Cossi, *J. Phys. Chem. A*, 1998, **102**, 1995–2001, DOI: 10.1021/jp9716997.

47 C. F. Riadigos, R. Iglesias, M. A. Rivas and T. P. Iglesias, *J. Chem. Thermodyn.*, 2011, **43**, 275–283, DOI: 10.1016/j.jct.2010.09.008.

48 T. Mandai, K. Yoshida, S. Tsuzuki, R. Nozawa, H. Masu, K. Ueno, K. Dokko and M. Watanabe, *J. Phys. Chem. B*, 2015, **119**, 1523–1534, DOI: 10.1021/jp508100s.

49 T. Mandai, K. Yoshida, K. Ueno, K. Dokko and M. Watanabe, *Phys. Chem. Chem. Phys.*, 2014, **16**, 8761–8772, DOI: 10.1039/c4cp00461b.

50 P. Johansson, J. Grondin and J.-C. Lassègues, *J. Phys. Chem. A*, 2010, **114**, 10700–10705, DOI: 10.1021/jp105437d.

51 L. Xue, C. W. Padgett, D. D. Desmarteau and W. T. Pennington, *Solid State Sci.*, 2002, **4**, 1535–1545, DOI: 10.1016/S1293-2558(02)00050-X.

52 CCDC 2488110: Experimental Crystal Structure Determination, 2026, DOI: 10.5517/ccdc.csd.cc2pj2my.